International Journal of Hydrogen Energy 136 (2025) 948–965

Contents lists available at ScienceDirect

International Journal of Hydrogen Energy

journal homepage: www.elsevier.com/locate/he

Enhanced CO_2 methanation over Ni-based catalysts: a comparative study on silica and alumino-silicate supports

Matteo Tommasi [a,b], Alice Gramegna [a,b], Alessandro Di Michele [c], Ermelinda Falletta [a], Federico Galli [d], Laura Prati [a], Ceri Hammond [e], Ilenia Rossetti [a,b,*]

[a] Chemical Plants and Industrial Chemistry Group, Dip. Chimica, Università degli Studi di Milano and CNR-SCITEC, Via C. Golgi 19, 20133, Milan, Italy
[b] INSTM Unit Milano-Università, Via C. Golgi 19, 20133, Milan, Italy
[c] Department of Physics and Geology, University of Perugia, Via A. Pascoli, Perugia, 06123, Italy
[d] Université de Sherbrooke, Département de génie chimique et de génie Biotechnologique, 2500 boul. de l'Université, Sherbrooke Québec, J1K 2R1, Canada
[e] Department of Chemical Engineering, Imperial College London, South Kensington Campus, London SW7 2AZ, UK

ARTICLE INFO

Handling Editor: Ibrahim Dincer

Keywords:
CO_2 methanation
Green hydrogen vector
Carbon dioxide utilization
Sabatier reaction
Synthetic methane

ABSTRACT

Various catalysts were prepared through wet impregnation of a Ni precursor. Different supports (SiO_2, SiO_2 Fumed and ZSM-5) and metal loadings were used, yielding catalysts with different specific surface area, metal support interaction and Ni dispersion. All catalysts showed the presence of a crystalline phase referable to NiO as precursor of the Ni active phase. SEM-EDX analysis confirmed a uniform distribution of the active phase on the support.

H_2-TPR analysis allowed to discriminate between two metal oxide reduction temperatures, indicative of metal dispersion and metal-support interaction strength. Provided that the overall peaks intensity increased with raising Ni loading, raising the Ni content led to a higher increase in intensity of a low reduction temperature peak with respect to higher temperature ones. This was attributed to weak interaction between the NiO and the support and bulker metal particles at high metal concentration. The reduction feature separated in two clearly identifiable reduction peaks for the samples with 45 wt% Ni loading.

Experimental tests conducted at atmospheric pressure showed very promising results for the catalysts with the highest Ni-loading with the Silica support. Significant differences between the use of SiO_2 and SiO_2 Fumed were found. SiO_2 Fumed supported materials showed a very high SSA, higher pore volume and bigger pore width compared to the other catalysts. A higher NiO reducibility was correlated for all tests with a higher activity towards CO_2 methanation. The bests results have been obtained with 36 wt% and 45 wt% Ni/SiO_2 Fumed. These materials showed the highest CO_2 conversion at 413 °C and 390 °C respectively, with 99 % selectivity towards methane in both cases. Of all of them, the 36 % Ni/SiO_2 Fumed allowed to achieve complete selectivity toward methane at about 390 °C. Ni/SiO_2 Fumed material showed extremely promising results when compared to catalysts reported in literature. Furthermore, the activity and selectivity obtained in the present work referred to a relatively high time factor (Qt/W of 60000 mL h^{-1} g_{cat}^{-1}), demonstrating the achievement of CO_2 conversions close to thermodynamic values at low temperatures, with full selectivity to methane under conditions where very high productivity can be obtained with small reactor volume. This leaves considerable room for optimizing operating conditions, to further improve the catalytic performances.

1. Introduction

4 ppm is the increase in atmospheric concentration of CO_2 over the past year that has brought the current concentration to about 425 ppm, compared to the 280 ppm of pre-industrial times. CO_2 is a greenhouse gas, able to have a dramatic impact on the climate. Tropicalization of the climate, melting of glaciers, droughts and rising seas are just some of the effects [1] impacting, for example, the economy of the agricultural

This article is part of a special issue entitled: ANM2024 (Titus) published in International Journal of Hydrogen Energy.

* Corresponding author. Chemical Plants and Industrial Chemistry Group, Dip. Chimica, Università degli Studi di Milano and CNR-SCITEC, via C. Golgi 19, 20133 Milan, Italy.
E-mail address: ilenia.rossetti@unimi.it (I. Rossetti).

https://doi.org/10.1016/j.ijhydene.2025.04.217
Received 1 January 2025; Received in revised form 20 March 2025; Accepted 11 April 2025
Available online 17 April 2025

sector [2]. Anthropogenic CO_2 emissions come mostly from the use of fossil fuels, with still 41 % of emissions coming from coal [3]. In 2023, emissions from energy production increased again by 1.1 % to a record 37.4 billion tons [4].

CO_2 emissions can be reduced in two ways. The first one is the use of renewable energy sources that intrinsically do not produce CO_2, such as solar, wind and hydro power. This first strategy is being applied increasingly widely, but there are still several energy-intensive, so-called "hard-to-abate" sectors whose electrification is extremely complicated and not yet economically feasible. In all these cases where CO_2 emissions are unavoidable, CCS (Carbon Capture and Storage) or CCU (Carbon Capture and Utilization) technologies come to help [5].

The latter is particularly interesting since it allows CO_2 to be transformed from waste to reagent, making it a C1 feedstock [6]. Enhanced Oil Recovery (EOR), direct use of CO_2 in food and medical sectors and production of synthetic fuel are just some of the utilizations of CO_2. An interesting solution that has become increasingly popular in recent years is to couple CO_2 utilization with hydrogen storage through catalytic CO_2 reduction reactions, such as methane and methanol synthesis or long-chain hydrocarbon production via Fischer-Tropsch [7–10].

Indeed, energy produced through renewable resources is intrinsically discontinuous. Peak energy production very often does not coincide with peak consumption required by the power grid and when there is excess electricity production, it can be stored in the form of renewable hydrogen. Green hydrogen has many advantages but the low volumetric density makes storage and transportation difficult [11,12]. Risk of hydrogen embrittlement in the natural gas pipelines makes the direct distribution of hydrogen impossible [13]. Many researchers claim that hydrogen will be the energy carrier of the future, due to its low environmental impact. However, the cost of hydrogen is currently extremely high. Most of the price comes from transport and storage costs [14,15].

At the current state of the art, the use of hydrogen in the catalytic hydrogenation reaction of CO_2 to methane seems increasingly appealing, allowing the coupling of the storage of green hydrogen with the use of CO_2, yielding a gaseous product that can be easily transported through the natural gas pipelines and applied by end users.

The CO_2-capture step, regardless of whether it is post-combustion capture, pre-combustion capture, or oxy-combustion, is not only complicated but especially expensive [16]. Recently, advanced trapping techniques based on adsorption on porous materials or the use of special membranes are being developed [17], but the maturity of this technology is still in its early stages. CO_2-DAC (Direct Air Capture) is not currently interesting as it is an inefficient and very energy consuming process [18].

An interesting idea, increasingly studied in recent years, is direct methanation of biogas, produced through anaerobic digestors (AD). ADs represents a widely adopted and mature technology [19]. Biogas consists of methane (35–65 %) and carbon dioxide (15–50 %). It also contains traces of other compounds such as hydrogen sulphide, nitrogen, oxygen and water vapour [20].

Direct biogas methanation can convert raw biogas into biomethane through reaction with hydrogen [21]. One of the main advantages of direct biogas methanation is the absence of CO_2 separation step. This contributes to the reduction of CO_2 emissions and avoids the cost associated with the CO_2 capture step, which positively impact the economics of the process [22].

The methanation reaction is currently commonly used to remove traces of CO and CO_2 in plants like ammonia production, where the catalyst is very sensitive to poisoning by oxygenates [23]. Direct hydrogenation of CO_2 is reported in Eq. (1). Alternative pathway is the carbon monoxide one where CO_2 is firstly transformed into CO though a Reverse Water Gas Shift (RWGS) reaction (Eq. (2)), which is later converted to methane (Eqs. (3) and (4)).

$$CO_2 + 4H_2 \rightleftarrows CH_4 + 2H_2O \quad \Delta H_{298K} = -164.9\ \text{kJ/mol} \qquad \text{(Eq. 1)}$$

$$CO_2 + H_2 \rightleftarrows CO + H_2O \quad \Delta H_{298K} = 41\ \text{kJ/mol} \qquad \text{(Eq. 2)}$$

$$CO + 3H_2 \rightleftarrows CH_4 + H_2O \quad \Delta H_{298K} = -206\ \text{kJ/mol} \qquad \text{(Eq. 3)}$$

$$2CO + 2H_2 \rightleftarrows CH_4 + CO_2 \quad \Delta H_{298K} = -247\ \text{kJ/mol} \qquad \text{(Eq. 4)}$$

Side reactions that lead to the formation of carbon deposits, such as the Boudouard reaction, need to be minimized or suppressed to retain a high selectivity towards methane. Deactivation of the catalyst due to coke deposition is also a problem when these reactions are present [24–26].

From a thermodynamic point of view, it is better to operate at the lowest possible temperature. In addition, in these conditions, theoretically the water formed by the methanation reaction is sufficient to prevent the formation of coke [27]. The H_2/CO_2 ratio in the feed is a crucial parameter. No advantage is reported while working with a ratio above 4, without taking into account the price of hydrogen, which significantly affects the total cost of the process [28,29].

Concerning the choice of the active phase initially used for this reaction [30], Mills et al. proposed a reduced classification of the metals according to their activity and selectivity [31].

Activity: Ru > Fe > Ni > Co > Mo.

Selectivity: Ni > Co > Fe > Ru.

A wide display of Ni-based catalysts is available in literature. Ni exhibits good selectivity and activity [32–34]. It is usually supported on materials with a high surface area (e.g. Al_2O_3) at high loading. A major advantage is its relatively low cost and availability, which makes it suitable for industrial applications [35]. One of the main requirements when using a Ni-based catalyst for performing methanation reaction is the use of a sulphur-free reactive mixture. H_2S acts as a poison, according to Eq. (5). The interaction of H_2S with NiO generates NiS and water, with loss of activity.

$$H_2S(g) + NiO(s) \rightleftarrows NiS(s) + H_2O(g) \qquad \text{Eq. 5}$$

Other sulphur containing compounds, such as thiophene, can react with hydrogen to give H_2S [36,37].

In recent years, many studies have been made to identify possible mechanisms for CO_2 methanation. Two mechanisms have been widely accepted. A so-called 'formate route' characterized by the associative adsorption of CO_2 and a second one characterized by the dissociative adsorption of CO_2, called 'CO route' [38].

The support contributes on an equal scale with the active phase to obtain a good catalyst. Not only it can give mechanical stability and resistance to sintering but it also allows the active component to be efficiently dispersed into small particles [39]. Oxygen vacancies, resistance to sintering, a high dispersion of the active phase compatibly with the high loading, are just some of the requirements that a Ni-based catalyst for CO_2 methanation must have [40]. Silica, has the advantage of having a high surface area and good thermal stability [41]. However, silica exploits weak interactions with the metal that can reduce the activity and facilitate sintering phenomena. In addition, coke deposition phenomena would appear to be easier on silica-based catalysts [42,43]. Zeolites, such as ZSM-5, are commonly used as industrial catalysts for processes such as cracking. They have the advantage of being thermally stable and having a large surface area. They have a unique porous structure and a tuneable acidity [44], which may affect the interaction with the active metal and with the reactant, and its high microporosity can tune reagent diffusion [45].

Based on the literature survey, insufficient reports are present on highly performing materials able to maximise CO_2 conversion and CH_4 selectivity in a low temperature regime. To fill this gap, the aim of this work is the study of silica and silico-aluminates (zeolites) as supports for Ni as active phase. The effect of support nature, its innocence towards the reaction, its interaction with the active metal and of metal loading have been explored for the methanation of CO_2. The catalysts have been characterized by N_2 adsorption/desorption, X-rays Powder Diffraction

(XRPD), Fourier Transform InfraRed spectroscopy (FT-IR), Diffuse Reflectance UV–Vis Spectroscopy (UV–Vis DRS), Raman Spectroscopy and Scanning Electron Microscopy couples with Energy Dispersive Spectroscopy (SEM-EDS) and tested at high time factor on a bench scale reactor at ambient pressure and variable temperature.

2. Experimental

2.1. Materials used

Two different silica supports were used in this work. The former is a silica produced by Sigma Aldrich, while the latter is SiO_2-Fumed produced by BDH Chemicals. Zeolite-based catalysts are widely used in industry, particularly in cracking and isomerization processes in the petrochemical industry. The support selected is zeolite ZSM-5 (ammonium form, CBV5524G) provided by Zeolyst. The material had a SiO_2/Al_2O_3 mole ratio of 50. $Ni(NO_3)_2{\cdot}6H_2O$ (Merck, 99 % purity) was used as precursor of the Ni active phase. All the gases used for the analysis (CO_2, H_2, He and N_2) were purchased from Air Liquide with purity >99.995 vol %.

2.2. Catalysts synthesis

Three catalysts were synthetized for each of the three supports selected, using different Ni loadings: 6 %, 16 %, 36 % (2 batches) and 45 % wt. A smaller samples set has been prepared for the less active samples series. The wet-impregnation (WI) technique was chosen for all the synthesis. WI has not only the advantage of being simple, fast and easily scalable, but also allows for the deposition of the active phase on the surface of the substrate, allowing reagents to easily contact the active phase. However, excessively increasing the metal loading decreases the dispersion and surface area of the final catalyst [46].

All the samples have been prepared according to a standardised procedure. $Ni(NO_3)_2{\cdot}6H_2O$ (Merck, 99 % purity) was used as precursor of the Ni active phase. 50 mL of water were used as solvent and the samples were all produced in batches of 3 g final product. The solvent was evaporated using a rotavapor. The impregnated compounds were placed in a static oven at 80 °C overnight prior to calcination.

Calcination was performed to oxidise the Ni precursor to NiO. The process was conducted in a tubular furnace (Carbolite GERO, model TF1 12/60/450). Air (40 mL min^{-1}) was flown to ensure the constant presence of oxygen and to eliminate NO_x formed during the process. Different calcination temperatures have been tested according to the type of support used, to minimize the possible negative impact of the high temperature treatment on catalyst activity, decreasing the surface area and porosity of the catalyst [47]. The Si-based samples have been calcined at 500 °C for 3 h with a heating ramp of 5 °C min^{-1} [48] while the catalysts supported over ZSM-5 were calcined at 550 °C for 6 h with a heating ramp of 1 °C [49].

2.3. Catalysts characterization

Numerous characterizations were conducted on all the as prepared and on some spent catalysts, as will be specified in the text.

All data related to porosity, surface area of both the catalysts and supports, were assessed with N_2-physisorption analysis. The latter have been performed with a 3Flex instrument by Micrometrics. Prior the analysis, ex-situ degas was performed at 200 °C under N_2 flow for 3 h.

Adsorption-desorption isotherms have been collected at −196 °C. The Brunauer-Emmett-Teller (BET) model has been used to calculate the surface area of the sample. The Barrett-Joyner-Halenda (BJH) method has been employed to quantify the pore size distribution in mesoporous materials [50]. The t-plot was used to quantify micropores area when relevant.

X-ray powder diffraction (XRPD) analysis was performed on all the synthetized catalysts using a MiniFlex – 600 – horizontal-scan powder diffractometer (Rigaku, Tokyo, Japan). Cu-Kα radiation was used with a graphite monochromator on the diffracted beam. Reflections observed in the XRPD pattern have been compared with the relative JCPDS cards. Crystal dimensions have been found using the Scherrer equation (Eq. 6),

$$D = \frac{K{\cdot}\lambda}{\beta{\cdot}\cos\theta} \quad \text{Eq. (6)}$$

where K is the shape factor (0.9), λ and β are respectively the X-ray wavelength (Cu Kα = 1.54 Å) and the FWHM (Full Width at Half Maximum), θ is the Bragg angle of the selected reflection and D is the calculated crystallite size.

The morphology of the catalysts surface has been studied by Scanning Electron Microscopy (SEM). Quantification of the active phase on the surface of the catalyst was carried out thanks to Energy Dispersive X-ray Spectroscopy (EDS). All the images have been acquired with a Zeiss LEO 1525 Field Emission Electron Microscope equipped with an Inlens detector, upon metallization with chromium and a Bruker Energy Dispersive X-ray Analyzer. Images have been collected at magnifications up to 500 k. EDS mapping has been performed on different spots for each catalyst. SEM images of all the samples are reported in the Supporting Information (SI) file. The SEM-EDS analyses were carried out on both the fresh samples and on selected spent catalysts after activity testing.

Fourier Transform InfraRed (FT-IR) spectra have been collected at wavenumbers between 4000 and 400 cm^{-1}. IR analysis relies on the Lambert-Beer law and provides important information on functional groups by investigating the bond typical vibrations. Spectra have been acquired with a FT-IR 4100 type A spectroscope from Jasco.

UV–Vis Diffuse Reflectance Spectroscopy (DRS) has been used to analyze solid samples to get information about the structure and conformation of active metals. UV–Vis DRS analyses were performed c/o Imperial College London using a UV-2600 from Shimadzu from 200 to 1000 nm. A blank with $Ba(SO_4)$ was carried out prior to analysis. Approximately 200 mg sample was analyzed.

Raman analyses were performed c/o Imperial College London using a Senterra II from Bruker. During each analysis, laser power, acquisition time, focus and magnification have been adjusted specifically for each material. A laser with λ equal to 532 nm has been used for all the analyses. When electromagnetic radiation is transmitted through a sample, a small fraction of the scattered radiation has λ different from that of the beam (Raman scattering), and this difference is determined by the chemical structure of the sample. The technique is extremely sensitive and also particularly useful for studying crystalline phases and structural defects (oxygen vacancies).

A Hiden CatLab Microreactor system was used to perform Temperature Programmed Reduction (TPR). A Mass Spectrometer gas analyzer (QGA) (Hiden Analytical) was used for the detection of outflowing species. 100 mg of catalyst were used for each analysis. A total flow of 50 mL min^{-1} (H_2/He ratio of 1:4 vol/vol) was used, with a heating ramp of 10 °C min^{-1} up to 500 °C, kept for 1 h m/z channels related to hydrogen (2) and water (18) were followed. Gaussian peak profiling allowed for an evaluation of the consumption of hydrogen. The area calculated was converted to mmol H_2 consumed through pulsed calibration performed with pure H_2.

Temperature Programmed Oxidation (TPO) and Temperature Programmed Desorption of pre-adsorbed oxygen (TPD-O_2) have been carried out on the same Hiden CatLab Microreactor. A first procedure (TPO-TPD mode1) consisted in a preliminary TPO by flowing 50 mL min^{-1} of air for 2 h over a sample of 50 mg of fresh catalyst, heating to 800 °C by 10 °C min^{-1}. Subsequently the gas was switched to 25 mL min^{-1} of He and the temperature was raised to 800 °C with a ramp of 10 °C min^{-1}.

A variation of this procedure (TPO-TPD mode2) consisted in pre-saturation of oxygen at 30 °C constant temperature by flowing 50 mL min^{-1} of air for 2 h over a sample of 50 mg of fresh catalyst. The following TPD was done as in the first TPD mode. The mass spectrometer was set to detect the *m/z* channels related to oxygen (32), water (18),

carbon dioxide (44), CO or N_2 (28) and the corresponding secondary masses with $m/z = 12, 14, 16$.

2.4. Experimental setup and activity testing

Equilibrium curves under each specific reaction condition have been calculated through the Aspen Plus® software using a Gibbs reactor, which minimises the Gibbs free energy of the reactants/products mixture. Pressure of 1 bar and a H_2/CO_2 ratio = 4 were considered, congruently with the testing conditions. Both Peng Robinson (PR) and Soave Redlich Kwong (SRK) have been used as equation of state (EoS). Equilibrium selectivities to methane and carbon monoxide have been calculated as well. The results obtained using Aspen Plus® were perfectly superimposable with those found in the literature [29].

All the activity tests have been carried out in a bench scale setup. The feed section was composed of calibrated MFCs (Brooks Instrument 5850 TR Series for N_2 and Brooks Instrument Delta Class) connected to the respective gas lines. A downflow tubular Inconel 800 reactor with an internal diameter of 9 mm was used, enclosed in a cast iron sheath and placed inside the oven. The oven was regulated by means of an Eurotherm (mod. 3204) controller. The temperature profile inside the reactor was measured through a movable thermocouple.

Water produced during the reaction was condensed and separated prior to GC analysis of the gaseous products.

During the tests the reactor was filled with quartz 10–20 mesh. The catalytic bed was isolated from the solid quartz by quartz wool wads.

Each catalyst was crushed and sieved (particle size 0.15 mm and 0.25 mm). 200 mg of meshed powder was used for each catalytic test after dilution with SiC 1:15 (wt/wt), to minimize hotspot formation due to the exothermicity of the reaction.

The in-situ activation was performed under pure hydrogen flow (40 mL min^{-1}) with an heating ramp of 5 °C min^{-1} up to 500 °C, kept for 1 h. After the activation the catalyst was cooled to 50 °C under inert flow and then the activity tests started. All tests have been performed with a total volumetric flowrate/weight (time factor) of the catalysts of 60000 mL g^{-1} h^{-1}. H_2/CO_2 were fed to the reactor with a molar ratio of 4.

Blank testing (i.e. without the catalyst) was conducted before starting the activity tests campaign and after as well. In both cases, a CO_2 conversion lower than 5 % at 550 °C was observed, with negligible methane formation.

An inline GC (Agilent 7890A) allowed to analyze the reacted mixture. The instrument, equipped with a 0.250 mL sampling loop and two columns (PLOTQ (19095P-Q04E) and molecular sieves (MS) (19095P-M56)), allowed to quantify CO_2, H_2, CO and CH_4 through a Thermal Conductivity Detector (TCD). He was used as carrier and N_2 as internal standard (IS). The use of an IS revealed fundamental to avoid overestimation of the gas concentration since the reaction takes place with a decrease in the number of moles (and thus volume).

2.5. Catalytic activity testing

The performances of the different catalysts were compared by evaluating the conversion of CO_2 (Eq. (7)), the selectivity towards CH_4 (Eq. (8)) and CO (Eq. (9)). F^0_{CO2} and F_{CO2} were the molar flow rates of CO_2 at reactor inlet and outlet, respectively.

$$CO_2\ Conversion\ \% = \frac{F^0_{CO_2} - F_{CO_2}}{F^0_{CO_2}} \times 100 \quad \text{(Eq. 7)}$$

$$CH_4\ Selectivity\ \% = \frac{mmol/min_{\ produced\ CH_4}}{mmol/min_{\ reacted\ CO_2}} \times 100 \quad \text{(Eq. 8)}$$

$$CO\ Selectivity\ \% = \frac{mmol/min_{produced\ CO}}{mmol/min_{reacted\ \ CO_2}} \times 100 \quad \text{(Eq. 9)}$$

Carbon balance was checked for every analysis. It is a point balance, where the amount of CO_2 entering (constant) and the amount of CO_2, CH_4 and CO quantified through GC at reactor outlet were compared. The general calculation used is reported in Eq. (10).

$$C\ balance = \left(\frac{mmol}{min}\right)^0_{CO_2} - \left(\left(\frac{mmol}{min}\right)_{CO_2} + \left(\frac{mmol}{min}\right)_{CH_4} + \left(\frac{mmol}{min}\right)_{CO}\right) \quad \text{(Eq. 10)}$$

3. Results and discussion

3.1. Catalysts characterization

Most of the characterization results represent the as prepared catalyst. Its activation was carried out in situ just before the reaction and after testing the sample was passivated by flushing inert gas and then a diluted oxygen containing mixture before discharging the reactor. This was due to the pyrophoric nature of reduced Ni and its capacity to adsorb and activate H_2. Consequently, analyses of the activated samples or of the spent catalysts would not be representative of the real working state. Furthermore, tested catalysts were diluted with SiC with high dilution ratio to prevent significant hot spot formation. The characterisation of spent catalysts was done only by SEM-EDS for these reasons.

3.1.1. N_2-physisorption analysis

The results of the N_2 adsorption-desorption tests are reported in Table 1 and interpreted according to the literature [51]. Adsorption and desorption isotherms for 36 % Ni/SiO_2 Fumed, 36 % Ni/SiO_2 Sigma and 36 % Ni/ZSM-5 are reported in Fig. 1 as an example. The results of all the supports and other catalysts tested are available in the Supporting Information (SI) (Figure SI 1.1 – SI 1.3).

Bare SiO_2 Fumed and ZSM-5 were both characterized by very high surface area, with values of 208 and 412 m^2 g^{-1}, respectively. The surface area of the SiO_2 Fumed support decreased as the metal loading increased, halving for metal loading of 45 wt% with respect to the bare support. The total pore volume also decreased when the Ni loading increased, due to the inclusion of NiO particles in the mesopores. In contrast, the pore width remained approximately constant, except few cases.

On the other hand, SiO_2 Sigma had an extremely low surface area (0.5 m^2 g^{-1}), due to the crystalline phase. Raman and XRPD analyses (*vide infra*) confirmed that the main phase of SiO_2 Sigma was cristobalite and the latter is characterized by very low surface area [52]. The surface area of the support was so low that increased after Ni addition, thanks to a porosity contribution of the Ni phase, though limited (Figure SI 1.2.E and 1.2.F).

Zeolite ZSM-5 showed the largest surface area and the surface area and total pore volume both decreased while the pore width increased, when increasing the Ni loading, as for the SiO_2 fumed series. All the ZSM-5 based materials showed a smaller average pore width compared to the SiO_2-Fumed one (ca. 6.5 nm for the former vs. ca. 30 nm for the latter). This is in line with the microporous uniform structure of the zeolite and the mesoporous one of the Silica-Fumed support, as confirmed by the pore size distributions reported in Fig. SI 1.1.G, 1.1.H, 1.3.G, 1.3.H. The significant increase of the pore width of the fumed silica samples series after Ni addition is correlated with the adsorption isotherm shape. While the pure support revealed very small, almost absent hysteresis, and a microporous feature was evident at low N_2 pressure, an H1 type hysteresis was present for all the Ni-loaded samples, with progressive suppression of the microporous features (Figure SI 1.1). This indicates specific mesoporosity induced by the formation of a Ni-containing phase. Ni addition also decreased the small contribution of micropores (14 m^2/g for the support, almost absent for the 36 % Ni/SiO_2 Fumed catalyst, Table 1).

All the isotherms reported in Fig. 1 and in Figure SI 1.1 – SI 1.3 of the SI were of type IV, indicating the presence of mesoporous structures, with significant microporosity only for the ZSM-5 samples. Furthermore,

Table 1
Main physical chemical properties of the prepared samples. Values in parenthesis for surface area refer to micropores calculated through t-plot.

Catalyst	BET_{SSA}[a] ($m^2\ g^{-1}$)	V_p[b] (cm^3/g)	P.W.[c] (nm)	Hysteresis	Ni loading[d] (%)	NiO size[e] (nm)
SiO_2 fumed	208 (14)	0.69	17.0	H1	–	–
6 % Ni/SiO_2 (fumed)	201	1.53	34.2	H1	11.7	15.5
16 % Ni/SiO_2 (fumed)	169	1.26	33.2	H1	16.2	14.6
25 % Ni/SiO_2 (fumed)	143	1.02	32.9	H1	24.6	15.1
36 % Ni/SiO_2 (fumed)	124 (0.7)	0.81	28.9	H1	32.7	13.4
45 % Ni/SiO_2 (fumed)	97	0.68	32.3	H1	43.2	15
SiO_2 Sigma	0.5	0.002	21.9	H3	–	–
6 % Ni/SiO_2 (Sigma)	2.2	0.009	13.5	H3	19.7	14.5
16 % Ni/SiO_2 (Sigma)	4.4	0.013	13.0	H3	24.8	16.1
36 % Ni/SiO_2 (Sigma)	10.1	0.030	13.5	H3	53.0	15.7
ZSM-5	412 (301)	0.107	6.0	H4	–	–
6 % Ni/ZSM-5	341	0.124	6.0	H4	6.3	10.9
16 % Ni/ZSM-5	253	0.106	6.6	H4	12.9	12.3
25 % Ni/ZSM-5	244	0.094	6.5	H4	19.1	15.9
36 % Ni/ZSM-5	197 (120)	0.092	7.3	H4	33.4	15.9
45 % Ni/ZSM-5	168	0.075	7.2	H4	35.9	19.0

[a] SSA = Specific Surface area.
[b] V_p = Total pore volume.
[c] P.W. = BJH Adsorption Pore Width.
[d] Ni loading from EDS.
[e] NiO Crystallite size from XRPD.

in Table 1 the types of hysteresis are classified according to IUPAC. The SiO_2 Fumed-based materials exhibit symmetrical adsorption and desorption paths, which indicates a very narrow distribution of mesopores (hysteresis type H1). SiO_2 Sigma based materials exhibited adsorption and desorption curves attributed to the presence of interstitial pores due to aggregates of particles sheets (hysteresis type H3). Finally, ZSM-5-based catalyst exhibits an H4 type hysteresis, which indicates the presence of micropores and their retainment after Ni addition.

3.1.2. XRPD

The XRPD patterns of the SiO_2 Fumed based materials are reported in Fig. 2. The materials were characterised as prepared since Ni after reduction can be pyrophoric. Therefore the catalyst was reduced in situ before activity testing and required passivation before discharging from the reactor. NiO was intended as precursor of the Ni active phase. The support showed a broad peak centred at about 22°, characteristic of amorphous silica [53]. The presence of this signal decreased as the nickel loading increased, while the typical NiO signals became progressively more intense. JCPDS no. 01-075-0269, related to the NiO phase was used as a reference and revealed the only Ni-containing phase. In particular, reflections were observed at $2\theta = 37°$, 43°, 63°, 75° and 79° that correspond to the crystalline planes of bulk NiO in cubic form indexed by (1 1 1), (2 0 0), (2 2 0), (3 1 1) and (2 2 2) planes, respectively [54,55].

SiO_2 Sigma based catalysts showed a completely different phase composition. The patterns are reported in Fig. 3. SiO_2 Sigma exhibited a well defined crystalline structure with reflections associated to cristobalite (JCPDS no. 00-039-1425). Cristobalite is a crystalline phase of silica obtained at high temperatures. The signals from the support were present at any loading and were very intense. Typical NiO reflections were also present in the catalysts.

The pattern of the commercial ZSM-5 substrate was consistent with the JCPDS chart no. 00-044-0003 for ZSM5, as reported in Fig. 4. In particular, the peaks at $2\theta = 7.9°$, 8.8°, 23.1° and 23.8° represent the (0 1 1), (0 2 0), (0 5 1) and (0 3 3) planes of the crystal structure, respectively [56].

Using the Scherrer equation, the average size of NiO crystallites was quantified. The results are summarised in Table 1. The β values were found using the peak fitting function of Origin software. Characteristic and non interfering reflections at $2\theta = 37°$, 43° and 63° were selected.

The average crystallite size remained about the same at each loading for the catalysts supported on silica: ca. 13–15 nm for those based on Fumed Silica and ca. 15 nm for those prepared on SiO_2 Sigma, despite the surface area difference by two orders of magnitude. Similarly, Zaho et al. reported an equal average crystallite size from 20 to 40 % loading of CoO_4 supported on SiO_2 [57]. On the contrary, catalysts supported on the zeolite material showed variable crystallite size, which increased from 10.9 nm of 6 % Ni/ZSM-5 to 19.0 nm of 45 % Ni/ZSM-5.

3.1.3. SEM-EDS

SEM-EDS analyses have been performed on all the synthetized materials and interpreted according to literature [58,59]. SEM images with the relative EDS mapping of 36 % Ni/SiO_2 Fumed, 36 % Ni/SiO_2 Sigma, 36 % Ni/ZSM-5 and 45 % Ni/SiO_2 Fumed are reported in Figs. 5–8 and Ni loading measured through EDS is reported in Table SI 2.1 and SI 2.2 (Supporting Information). SEM images, together with EDS mapping, of all the other supports and catalysts tested are available in the Supporting Information (SI) (Figures SI 2.1 – SI 2.16).

SiO_2 Fumed (Figure SI 2.1) appeared as an agglomeration of spheroidal nanoparticles with an average diameter of approximately 10–20 nm, in line with data reported in literature [60]. SEM images of 36 % Ni/SiO_2 Fumed (Fig. 5) did not allow the distinction of any NiO-related structures on the surface of the sample, showing a morphology similar to that of the support. However, EDS analysis confirmed Ni presence. Finally, the mapping showed a homogeneous distribution of NiO on the support. Looking to the evolution of morphology with Ni loading, one may conclude that the support shape and size was retained during metal addition, but some whiskers became evident at very high metal loading (36 and 45 wt%). A first hypothesis was that Ni was in part agglomerated in the form of Ni-whiskers. Another option is that carbon nanotubes may have formed from Ni particles, but a C-based precursor that may significantly feed the growth of C-nanotubes was not present during catalyst synthesis. The former hypothesis remains the most likely.

The formation of Ni whiskers is well supported in the literature, though the mechanism of formation and growth is not fully understood. Metal whiskers are commonly formed over metal surfaces and metal coatings and they have been also widely reported on ceramic oxides and, as a specific case of interest for this work, for NiO [61,62]. Their formation has been initially correlated to the presence of tensile strength, that relaxed through the extrusion of a filament. More in general, the phenomenon rises from a high energy state of the metal or metal oxide,

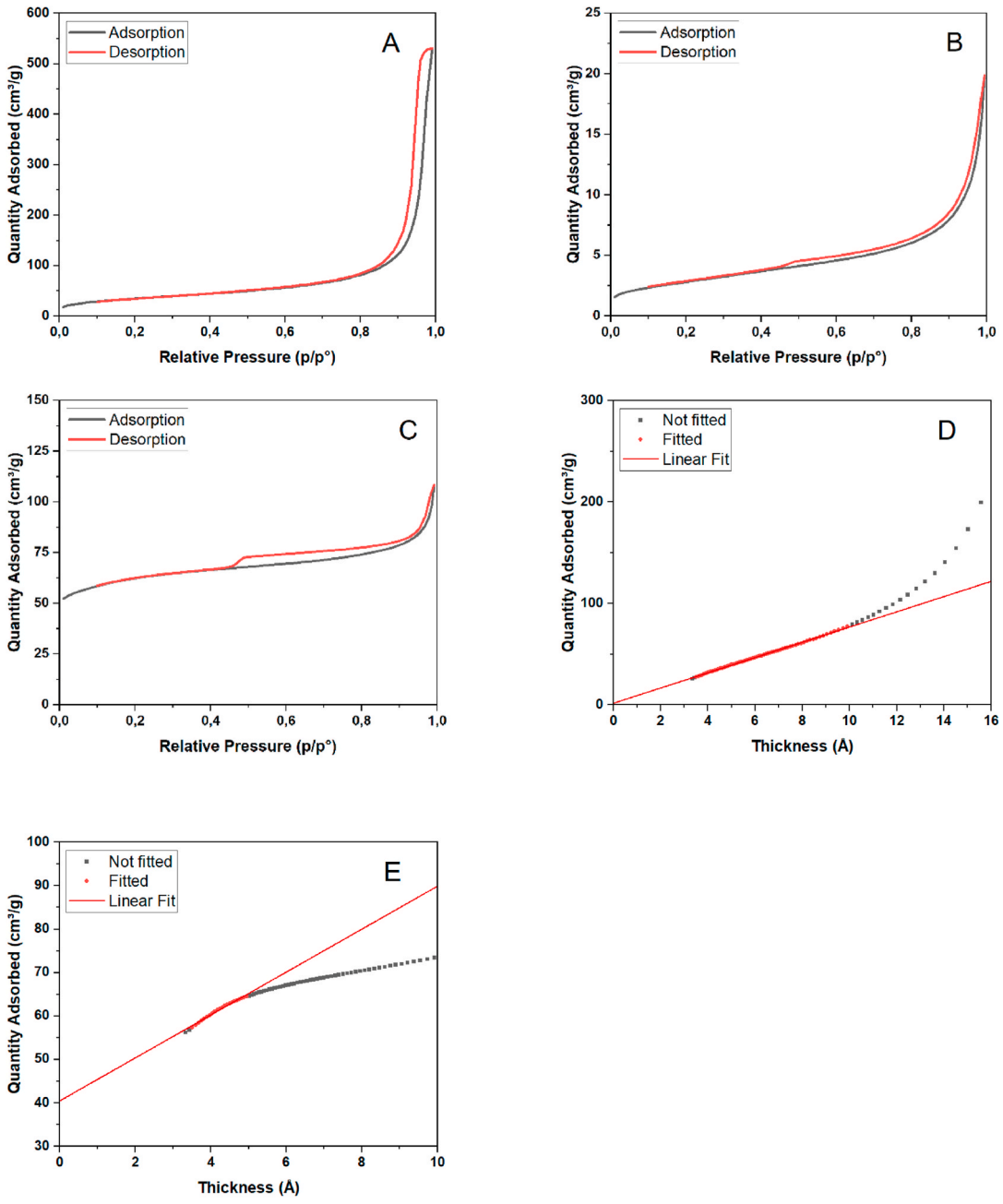

Fig. 1. Adsorption and desorption isotherms for: A) 36 % Ni/SiO_2 Fumed; B) 36 % Ni/SiO_2 Sigma; C) 36 % Ni/ZSM-5; D) t-plot 36 % Ni/SiO_2 Fumed; E) t-plot 36 % Ni/ZSM-5.

which evolves in a lower energy state through formation of a filamentous protrusion. The growth is accelerated by temperature and thus it can be hypothesized that NiO whiskers formed during calcination of the precursor [63,64]. High dispersion and strong interaction with the support inhibit the formation of whiskers, while bulkier particles are more prone to filaments formation. This has been reported e.g. for NiO/Silica SBA-15 [65].

The SiO_2 Sigma support (Figure SI 2.7) on the other hand, showed the presence of very large support grains. The latter indicates the presence of large crystallites, as confirmed by the mapping study and in agreement with XRPD data for cristobalite. After Ni addition, smaller regularly shaped pseudo-octahedral particles appeared, with variable size, often higher than 100 nm.

The EDS mapping images of the 36 % Ni/SiO_2 Sigma (Fig. 6) confirmed that Ni particles were finely dispersed over the entire surface of the catalyst. The mapping study of samples at different Ni loading (Figure SI 2.9) also showed geometrically regular structures of different sizes, characteristic of Ni oxide. No sign of whiskers was evident for this support, even at high metal loading.

SEM-EDS images of ZSM5-based materials are reported in Figures SI 2.11-SI 2.16. ZSM-5 (Figure SI 2.11) showed a very regular and homogeneous pseudo-cubic morphology, with particles ranging from ca. 200 to ca. 400 nm. The EDS mapping assessed a quite homogeneous distribution of NiO on the surface of ZSM5, as observed in the 36 % Ni/ZSM-5 mapping shown in Fig. 7 and in related images in the Supporting Information file. EDS analyses, moreover, confirmed the presence of Al, (the starting material has a SiO_2/Al_2O_3 mole ratio of 50). Smaller particles with spherical shape (ca. 10–20 nm) were evidenced over the zeolite surface at low metal loading, evolving into regular octahedra at higher metal loading. For this support, no formation of Ni whiskers was

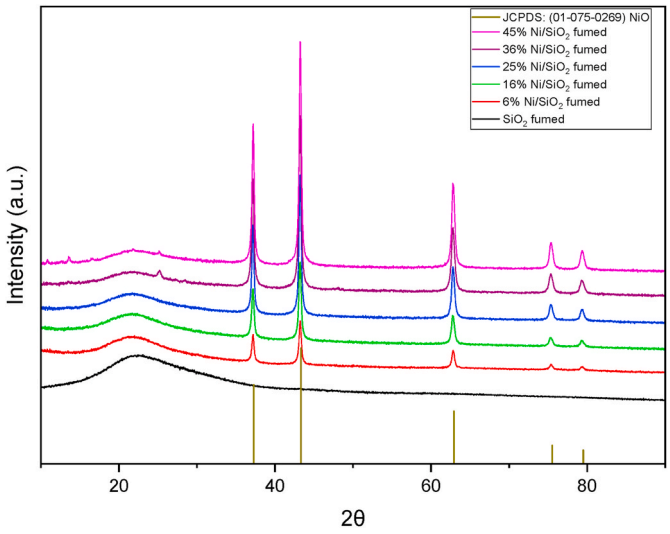

Fig. 2. XRPD pattern of the SiO_2 Fumed supported catalysts.

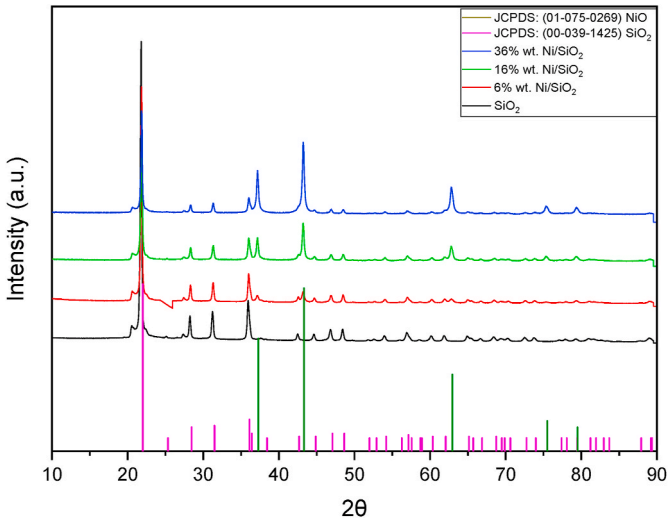

Fig. 3. XRPD pattern of the SiO_2 Sigma supported catalysts.

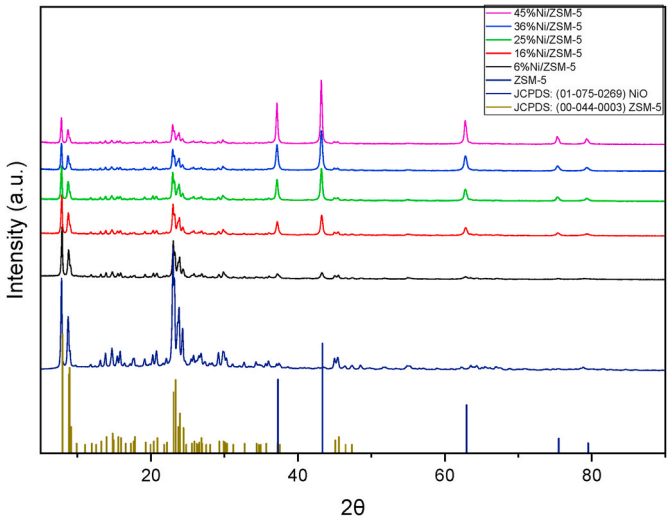

Fig. 4. XRPD pattern of the ZSM-5 supported catalysts.

evident at any loading.

Though it is not the focus of this work, it may be interesting to highlight that the most stable geometrical arrangement of NiO is in octahedral particles [66], which were indeed observed for the SiO_2 Sigma and the ZSM-5 supports at high metal loading. The growth of the most stable morphology was not observed in the case of SiO_2 fumed. Deviations from the octahedral morphology were reported as higher energy forms of NiO particles, also in case characterized by variable magnetic and optoelectronic properties [66–70]. Filamentous growth of NiO was reported for various techniques of film growth, e.g. Ref. [71]. An hypothesis for this different NiO growth over different supports in the present case may be as follows. The high surface area of ZSM-5 is substantially ascribed to micropores. The finest are inaccessible for the Ni precursor, while it can possibly penetrate the widest ones, as testified by the evolution of the surface area of the ZSM-5 supported samples at increasing metal loading. Therefore, after saturating the accessible pores, further increase of Ni loading brings to Ni accumulation over the surface. The low surface area and porosity of the SiO_2 Sigma led to NiO accommodation over the support surface, only. In both cases the spontaneous growth of the most stable shape is expected, as visible in the formation of octahedral particles over both supports at high Ni loading.

Fumed silica rapidly lost its (smaller) microporous contribution and accommodated the Ni precursor over the small spherical nanoparticles with film growth, i.e. at higher energy form with respect to octahedral particles. This may explain why filaments formed at high loading, to decrease the overall system energy.

Ni actual concentration is reported in Table SI 2.1 and SI 2.2 (Supporting Information) and in general, the Ni loading values had an increasing trend with higher loading and were similar to the theoretical ones. This was strictly confirmed in the case of SiO_2 Fumed based materials. In contrast, the values for SiO_2 Sigma were much higher than the theoretical ones. This could be due to the fact that SiO_2 Sigma has a low surface area and pore volume. Ni will only be deposited on the surface, not entering the pores, therefore causing an enrichment of NiO on the surface, with overestimation of NiO concentration, being EDS analysis more sensitive to the surface composition even if it is not a surface technique in strict sense [72]. On the opposite side, the actual Ni loading for the zeolite-supported materials was underestimated. In this case the deposition of Ni inside the pores is also verified by the sensitive decrease of surface area, preventing an accurate detection by EDS.

Exactly as in the case of the 36 % Ni loaded sample, the 45 % Ni/SiO_2 Fumed material (Fig. 8) did not evidence any NiO-related structures on the surface and EDS analysis confirmed once again an homogeneous dispersion of the NiO, with a morphology similar to the one of the bare material, except for the presence of whiskers.

3.1.4. FT-IR

FT-IR spectra of all SiO_2 Fumed based materials showed a very intense broad band around 3500 cm^{-1} and a further band of lower intensity at ca. 1625 cm^{-1} (Fig. 9). Both bands were associated with O–H bonds (stretching the former, bending the latter). The band at 1385 cm^{-1} can be associated with C–H bond bending vibrations of organic substances in the samples, which should not be present. Alternatively such band is typical of nitrate ions bending vibrations, which is much more likely index of not completely decomposed Ni precursor or to the bending of surface OH groups [73,74]. Interestingly, this band is visible only for the silica fumed catalysis with 36 and 45 wt% Ni loading, i.e. the ones showing the whiskers in their SEM micrographs. This can support either that the whiskers were constituted of Ni oxide with residual nitrate precursor. Alternatively, it may be compliant with the presence of carbon nanotubes, which however would not include significant amount of H, being mainly composed of C. Accordingly, it may also be due to Ni hydroxylated sites on the surface as detailed in Ref. [75]. The latter is considered the most likely attribution, useful also to explain the high activity of the sample loaded with 36 and 45 wt% of Ni.

The bands at 1100 cm^{-1} and 800 cm^{-1} and 460 cm^{-1} are attributable

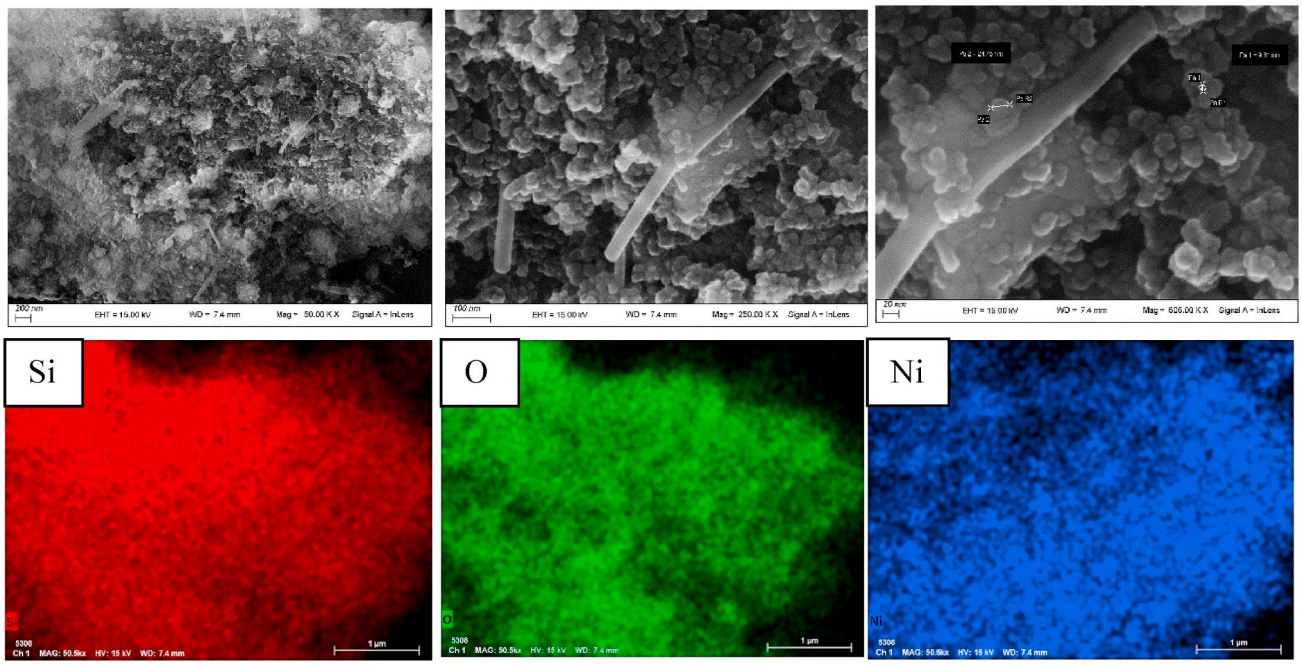

Fig. 5. SEM-EDS images, Si, O and Ni mapping of 36 % Ni/SiO_2 Fumed. Marker size: top row from left to right 200 nm, 100 nm, 20 nm. Bottom row 1 μm.

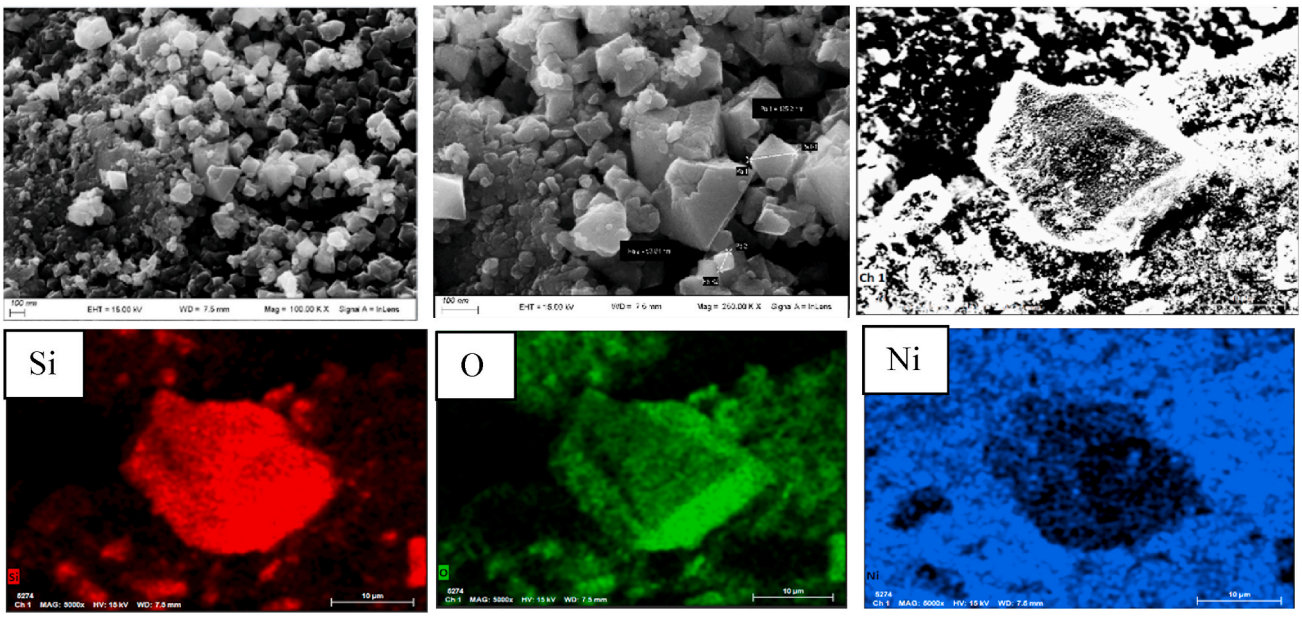

Fig. 6. SEM-EDS images, Si, O and Ni mapping of 36 % Ni/SiO_2 Sigma. Marker size: top row from left to right 100 nm, 100 nm, 10 μm. Bottom row 10 μm.

to the asymmetric and symmetric stretching of the Si–O bond [76]. The band at 460 cm^{-1} is also attributable to the stretching of the Ni–O bond. The positions of the Si–O and Ni–O stretching bands are very similar and this causes an overlapping, making impossible their exact identification.

In the case of SiO_2 Sigma (Fig. 10), the bands previously assigned were present as well. A slightly different shape and position of the bands was observed. This indicates the presence of particles of different shapes and/or sizes. In particular, a red shift is observed which indicates the presence of larger particles [77]. This has been confirmed by SEM analysis. The band at 1385 cm^{-1} was not present for this support and was barely visible, though not significant for any Ni-containing sample. This would confirm its attribution to some residual nitrate.

The FT-IR spectra reported in Fig. 11 showed the characteristic bands of ZSM-5. Absorption bands at 451 cm^{-1}, 545 cm^{-1}, 795 cm^{-1}, 1198 cm^{-1} and 1220 cm^{-1} are attributable to the bending vibration of the T-O bond (T = Al or Si), symmetrical external O-T-O stretching, asymmetrical internal and external stretching vibrations due to the presence of siliceous materials [78]. A small band at 1385 cm^{-1} was already present in the bare support, associated with C–H bond vibrations of organic substances present in the samples as impurities coming from the template used for the synthesis of the zeolite or to OH bending vibrations. Its intensity never became significant, except at high metal loading. The broad bands between 3130 cm^{-1} and 3650 cm^{-1} can be attributed to the vibrational stretching of isolated Si–OH and Al–OH groups and O–H of water molecules [78]. In addition to these signals, the higher NiO-loaded sample showed an intense absorption band at 450 cm^{-1},

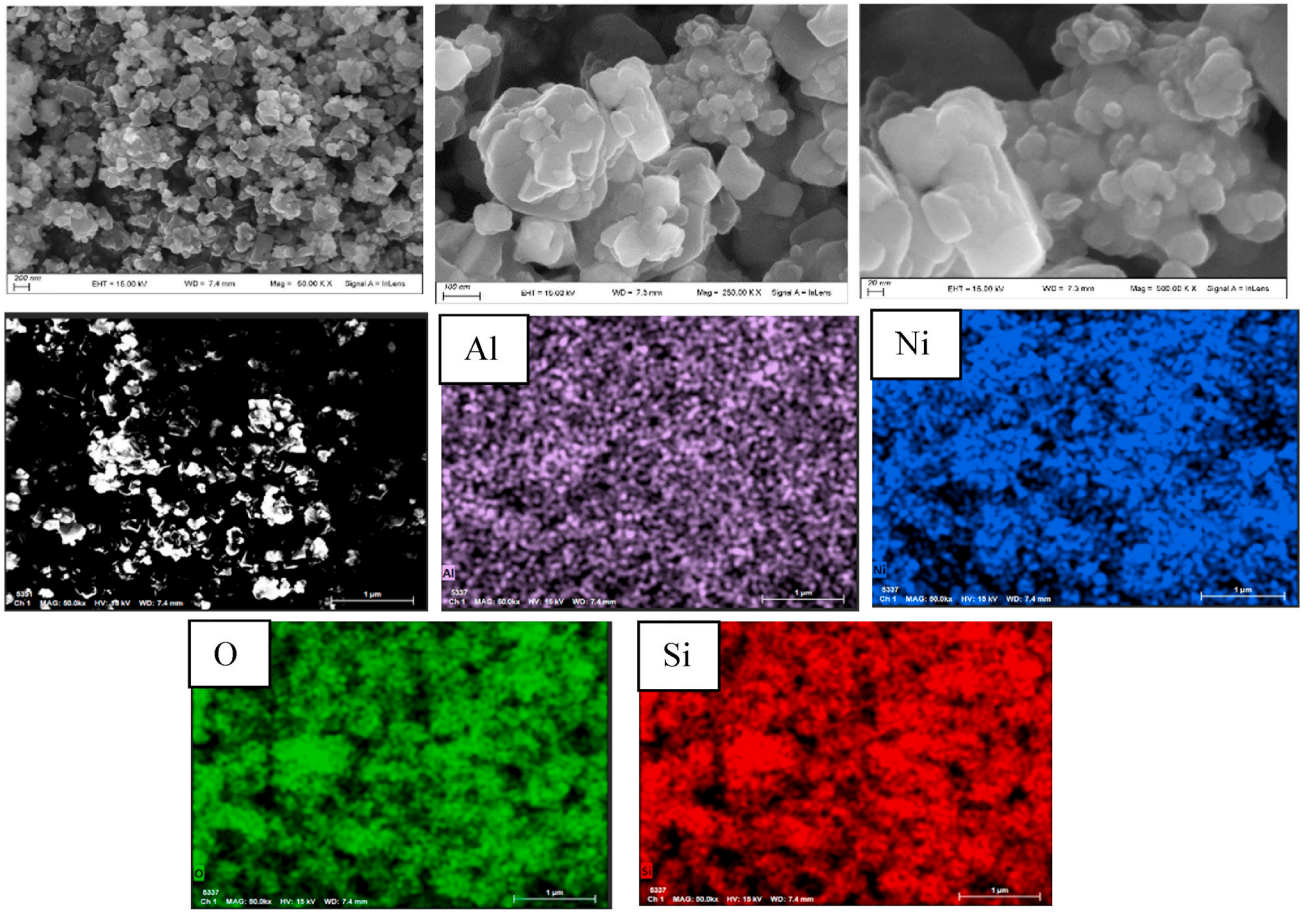

Fig. 7. SEM-EDS images, Si, Al, O and Ni mapping of 36 % Ni/ZSM-5. Marker size: top row from left to right 200 nm, 100 nm, 20 nm. Second and third rows 1 μm.

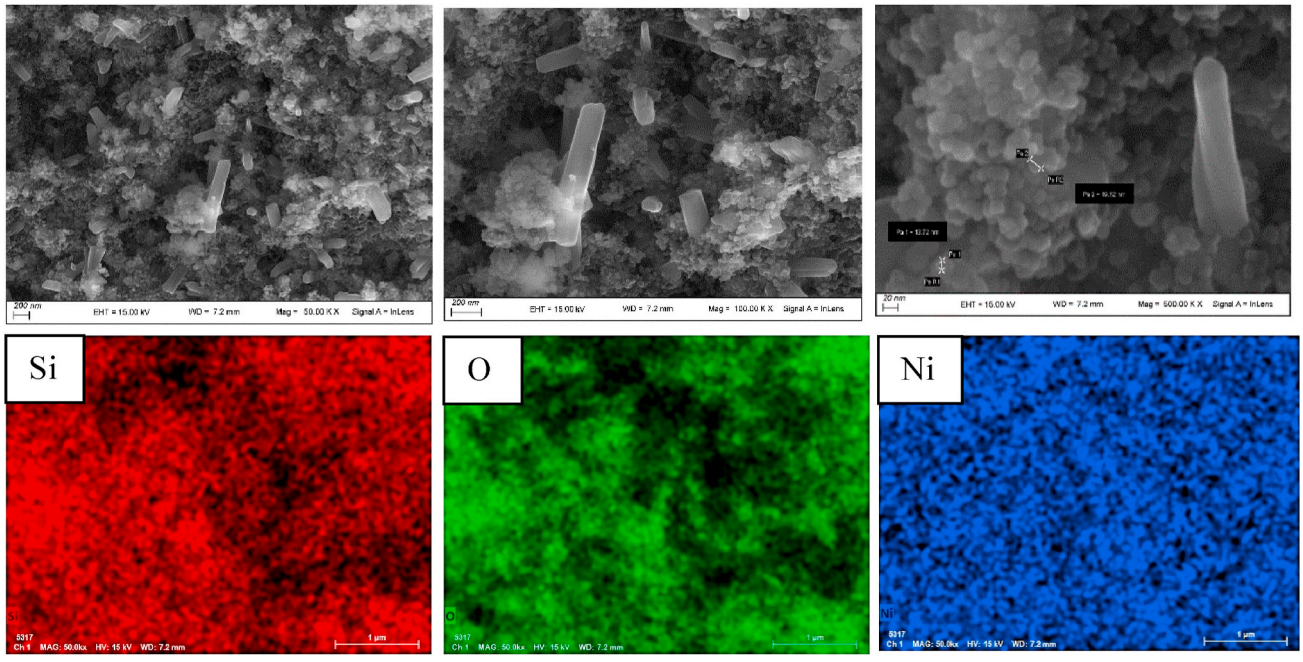

Fig. 8. SEM-EDS images, Si, O and Ni mapping of 45 % Ni/SiO_2 Fumed. Marker size: top row from left to right 200 nm, 200 nm, 20 μm. Bottom row 10 μm.

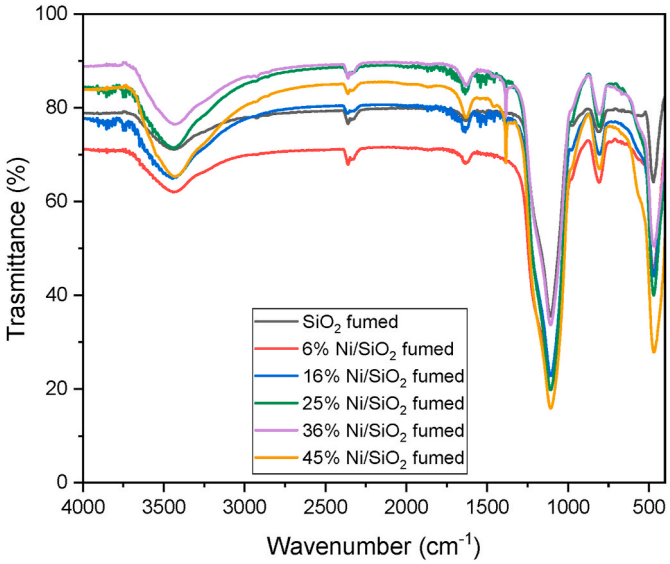

Fig. 9. FT-IR spectra of the SiO_2 Fumed supported catalysts.

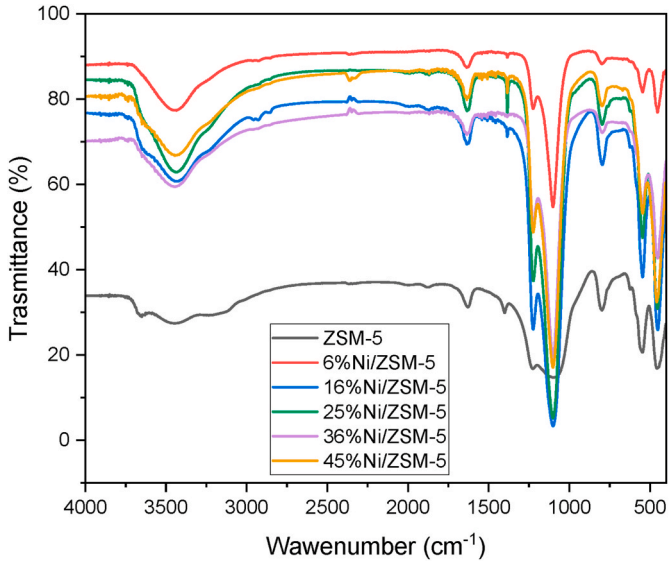

Fig. 11. FT-IR spectra of the ZSM-5 supported catalysts.

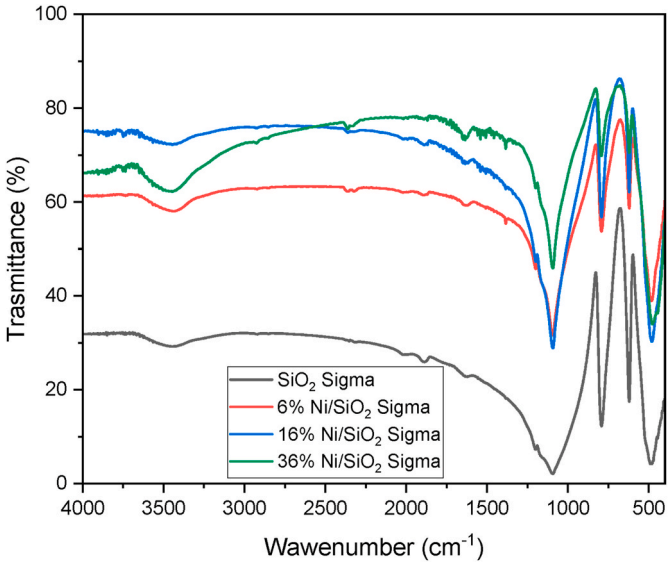

Fig. 10. FT-IR spectra of the SiO_2 Sigma supported catalysts.

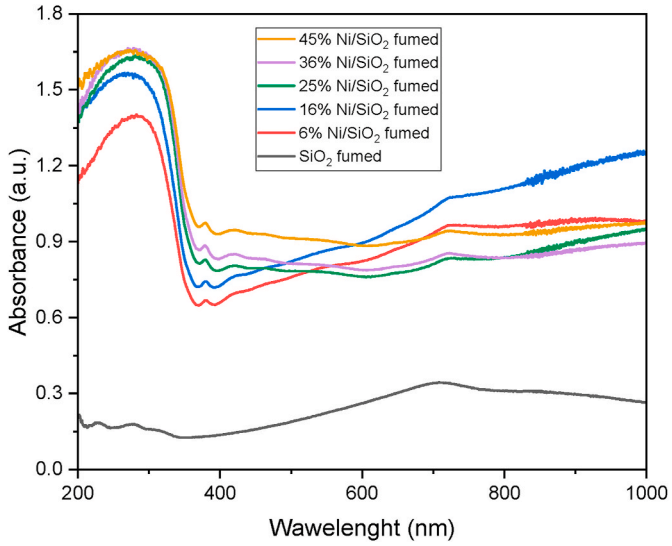

Fig. 12. UV–Vis DRS spectra of the SiO_2 Fumed supported catalysts.

which is characteristic of the vibrational stretching of the Ni–O bond. In low loading samples, the NiO band was not visible due to the overlapping with the support band. Moreover, the exact position of this band was reported to vary depending on the particle size and the shape distribution of NiO particles [79].

3.1.5. UV–Vis DRS

Figs. 12 and 13 showed the UV–Vis-DRS spectra of the SiO_2 Fumed and the SiO_2 Sigma materials respectively. All the catalysts exhibited bands at 270 nm, 380 nm, 420 nm and 720 nm, all characteristic of NiO species, except the latter, present in the bare support. The low loading samples had an absorbance increase at high wavelength resembling the bare support. The absorbance of the Ni loaded samples at low wavelengths was instead increasing progressively with Ni loading.

In Fig. 14 the UV–Vis DRS spectra of the ZSM-5 based materials are reported. All the catalysts exhibited bands at 270 nm, 380 nm, 420 nm and 720 nm, characteristic of the NiO species [80]. The 270 nm band is assigned to the charge transfer $O^{2-} \rightarrow Ni^{2+}$ between the metal and the support [81]. The bands at 380 nm, 420 nm and 720 nm are assigned to d-d electronic transitions of Ni^{2+} in octahedral coordination within NiO [82]. The literature reports also the presence of bands centred at 450 nm and 635 nm that correspond to d-d electron transitions of Ni^{2+} exchanged in tetrahedral coordination within the zeolite structure [83]. These bands were weakly present also in the high-loading sample. This could indicate that the insertion of Ni into the zeolite structure occurred only with large amount of metal. At higher Ni loading, absorption increased and the bands were more intense.

3.1.6. Raman

Raman spectra for SiO_2 Fumed based materials are reported in Fig. 15. SiO_2 Fumed did not reveal any Raman signal. Despite this, even at low loadings, NiO bands were noticeable. These were slightly shifted to lower wavenumbers, due to small crystallite sizes [84]. Finally, the high intensity of the 1P band suggests that NiO is antiferromagnetically ordered or defect-rich [85].

The spectrum of the bare SiO_2 Sigma (Fig. 16) showed bands at 113 cm^{-1}, 230 cm^{-1}, 420 cm^{-1}, 780 cm^{-1} and 1070 cm^{-1} that were attributed to cristobalite [52,86]. The bands were also visible in the 6 % sample, but disappeared at high loadings. The peaks related to the

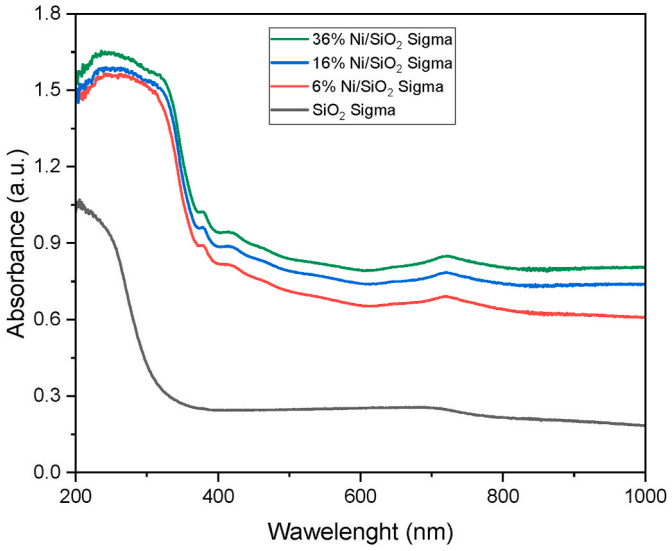

Fig. 13. UV–Vis DRS spectra of the SiO_2 Sigma supported catalysts.

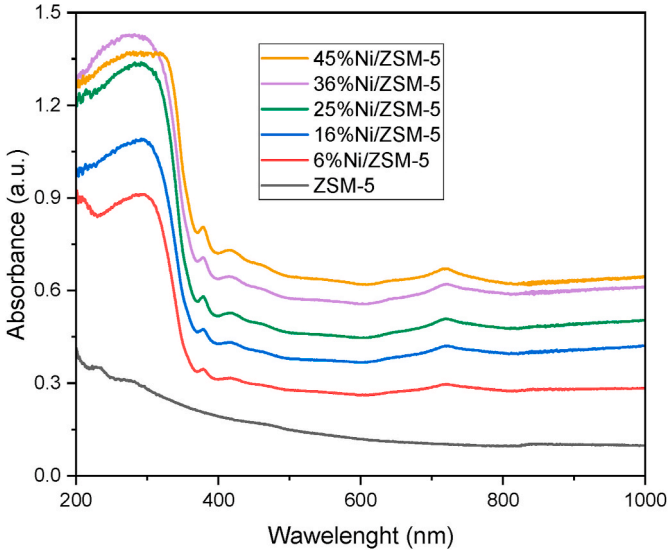

Fig. 14. UV–Vis DRS spectra of the ZSM-5 supported catalysts.

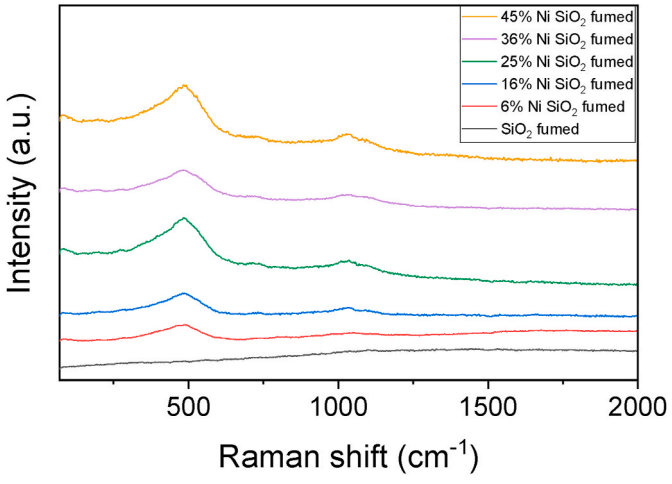

Fig. 15. Raman spectra of the SiO_2 Fumed supported catalysts.

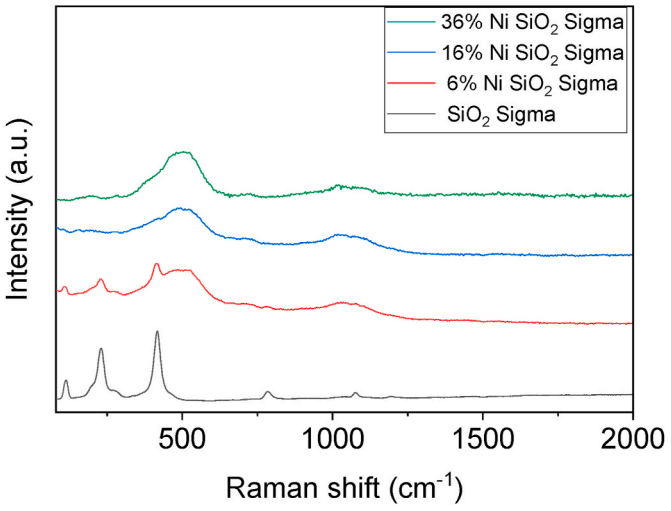

Fig. 16. Raman spectra of the SiO_2 Sigma supported catalysts.

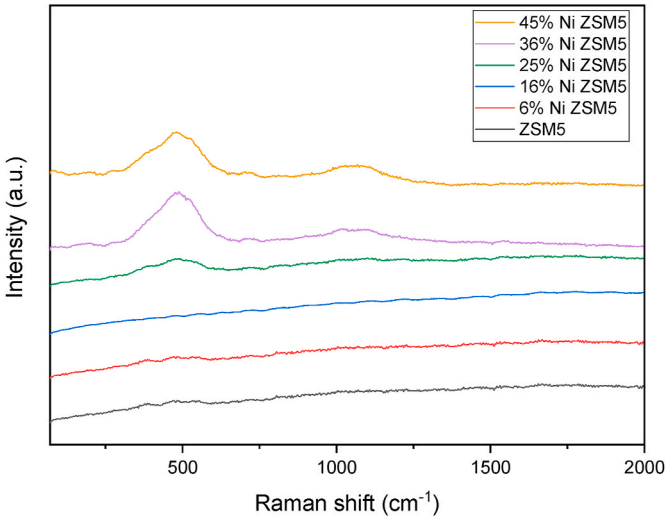

Fig. 17. Raman spectra of the ZSM-5 supported catalysts.

presence of NiO appeared in the metal loaded catalysts.

Fig. 17 shows the Raman spectra for ZSM-5 based materials. The bare zeolite did not show any Raman signal. Typical NiO bands appeared with metal addition. It is reported in the literature that the NiO Raman spectrum has five main bands. The band at 570 cm^{-1} that correspond to one-phonon (1P) TO and LO modes, a band at ca. 730 cm^{-1} that corresponds to two-phonon (2P) 2TO modes, a band at 900 cm^{-1} that corresponds to + LO, a band at 1100 cm^{-1} that corresponds to 2LO modes and finally, a band at 1490 cm^{-1} that corresponds to two-magnon (2 M) scattering [85]. The 2P bands at 900 cm^{-1} and the 2 M bands at 1500 cm^{-1} were not present. This is probably due to the very small size of the crystallites [84]. The spectra obtained showed an increasing intensity of the bands as Ni loading increased and this may be due to the increase in crystallite size [87]. The high intensity of the 1P band at 570 cm^{-1} suggests that NiO is antiferromagnetically ordered or defect-rich [88], likely due to surface oxygen vacancies [89].

3.1.7. H_2-TPR, TPO and TPD-O_2

All TPR analysis are shown in Fig. 18 and Figures SI 3.1 – SI 3.13 of the SI. For all the series, increasing the Ni-loading translated into increasing the mmol of H_2 consumed, as reported in Table 2. All the series displayed a decreasing trend in the reduction temperature while

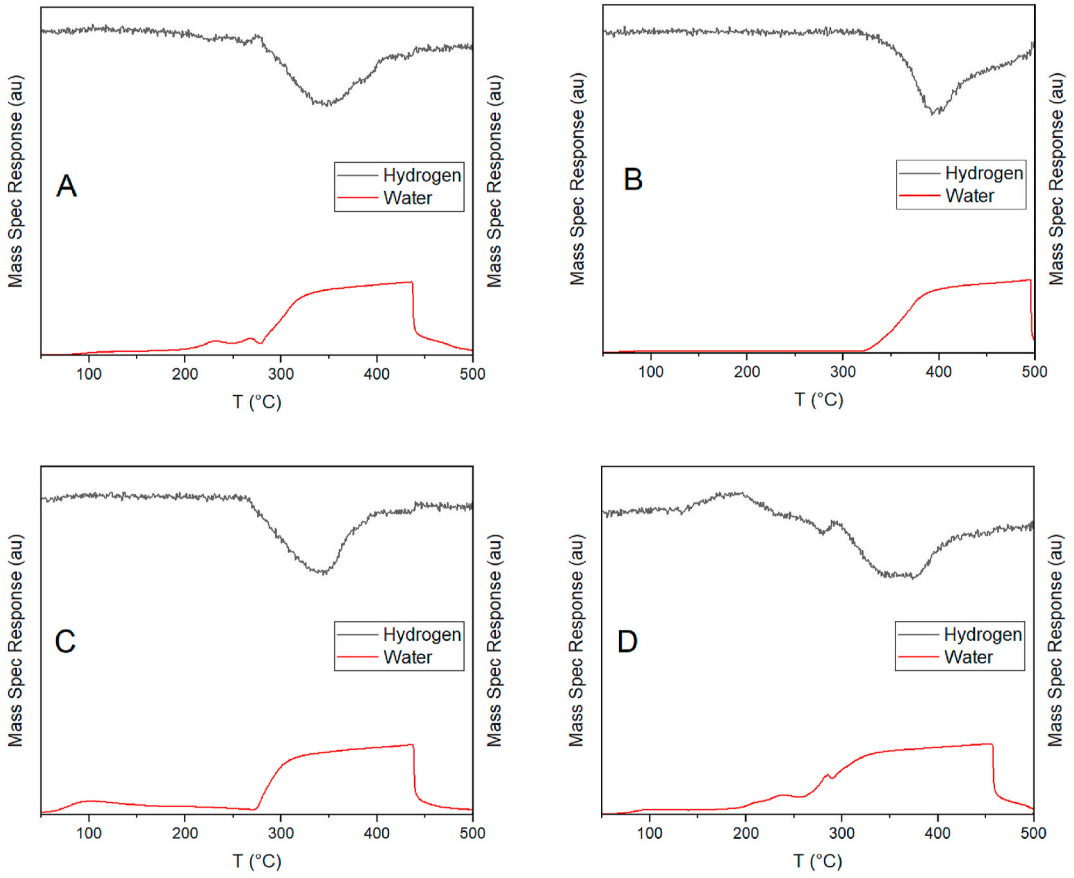

Fig. 18. H_2 – TPR of: A) 36 % Ni/SiO_2 Fumed; B) 36 % Ni/SiO_2 Sigma; C) 36 % Ni/ZSM-5; D) 45 % Ni/SiO_2 Fumed.

Table 2
H_2-TPR characterization results: amount of H_2 consumed (total) and reduction peak temperatures.

Catalyst	H_2 (mmol)	$T_{Peak\ 1}$ (°C)	$T_{Peak\ 2}$ (°C)
6 % Ni/SiO_2 Sigma	2.44E-01	440	
16 % Ni/SiO_2 Sigma	1.38E+00	418	
36 % Ni/SiO_2 Sigma	2.86E+00	395	
6 % Ni/SiO_2 fumed	2.27E-01	440	
16 % Ni/SiO_2 fumed	1.11E+00	378	
25 % Ni/SiO_2 fumed	1.67E+00	374	
36 % Ni/SiO_2 fumed	2.31E+00	345	
45 % Ni/SiO_2 fumed	2.62E+00	280	357
6 % Ni/ZSM-5	3.01E-01	356	
16 % Ni/ZSM-5	1.32E+00	317	
25 % Ni/ZSM-5	1.74E+00	354	
36 % Ni/ZSM-5	2.45E+00	341	
45 % Ni/ZSM-5	2.93E+00	279	370

increasing the loading of Ni. For various supports, it is widely accepted in the literature that lower reducibility (i.e. higher temperature reduction peaks) is correlated to high dispersion and/or strong metal/support interaction and viceversa. Independently from the support nature, the presence of various peaks at a given loading is likely due to NiO species that interact differently. Weak interactions between the NiO and the support are responsible of the peaks at lower T while strong metal/support interactions (SMSI) are responsible for the reduction peaks at higher temperature [90,91].

When looking for instance at the 45 % Ni/ZSM-5 and 45 % Ni/SiO_2 Fumed samples, two reduction peaks were clearly visible for both samples, at 280 °C–357 °C for the 45 % latter and 279 °C–370 °C for the former. The peak at lower temperature may be also related to a higher availability of surface Ni [91].

In the respective samples having 36 % nickel loading, the contribution of the two peaks was also observable, but not noticed in the 36 % Ni/SiO_2 sample, for which a less pronounced temperature decrease was attained.

TPD of preadsorbed oxygen was used to assess the presence of oxygen vacancies in the samples. Therefore, the sample was pre-saturated in flowing air according to two procedures. The former consisted in a TPO (TPO-TPD mode 1), which also allowed to identify possible carbonaceous residua or oxygen consumption due to significant oxidation of the catalyst precursor.

The TPO pattern of sample 45 % Ni/SiO_2 Fumed revealed the continuous consumption of oxygen in the whole temperature range and the specific release of fragments with *m/z* 44 and 18 attributed to CO_2 and H_2O between ca. 200 and 300 °C. The same results were observed for sample 36 % Ni/SiO_2 Fumed in the temperature range 170–300 °C. In all the cases the intensity of the peaks was very small, as evidences in Figures SI 3.14A and SI 3.14B. This indicates likely the combustion of very small amounts of organic compounds present in the sample.

Nevertheless, the TPD analysis did not reveal any oxygen release after TPO at high temperature. Therefore the pre-saturation procedure was changed to a treatment in air at near ambient temperature (30 °C, TPO-TPD mode2). A release of oxygen was observed after such saturation, corresponding to very small peaks evident between 200 and 300 °C both in the *m/z* signals 32 and 16. An example is reported in Figure SI 3.15 and was attributed to the presence of oxygen vacancies.

3.2. Catalytic tests

All catalysts tested, irrespectively of the supports, showed a general increase in activity as Ni loading increased. In general, SiO_2 Fumed

supported catalysts exhibited the highest activity.

The max CO_2 conversion (together with the T at which it has been obtained and the corresponding methane selectivity, S CH_4) and the max CH_4 selectivity (together with the T at which it has been obtained and the corresponding CO_2 conversion) are reported in Table SI 4.1. In some cases the optimum temperature was coincident for conversion and selectivity maximization. The carbon balance has been calculated for every experiments. All tests showed a carbon balance of 95 % or higher.

As a general trend, as the Ni loading increased the conversion increased as well and the temperature of best achievement decreased. Low loading samples were not able to attain full selectivity to methane, the main byproduct being CO.

Considering the ZSM-5 supported series, the 45 % Ni/ZSM-5 sample showed the highest CO_2 conversion (71 %) of the series at 450 °C, while still displaying 95 % selectivity towards methane, as reported in Table SI 4.1. Fig. 19a and b represent more in detail the conversion and selectivity of catalysts supported on ZSM-5 and compare the results with the expected thermodynamic conversion at equilibrium (azure curve labelled "THERMO"). By increasing the loading of the active metal, there is an increase in both conversion and selectivity, which is in line

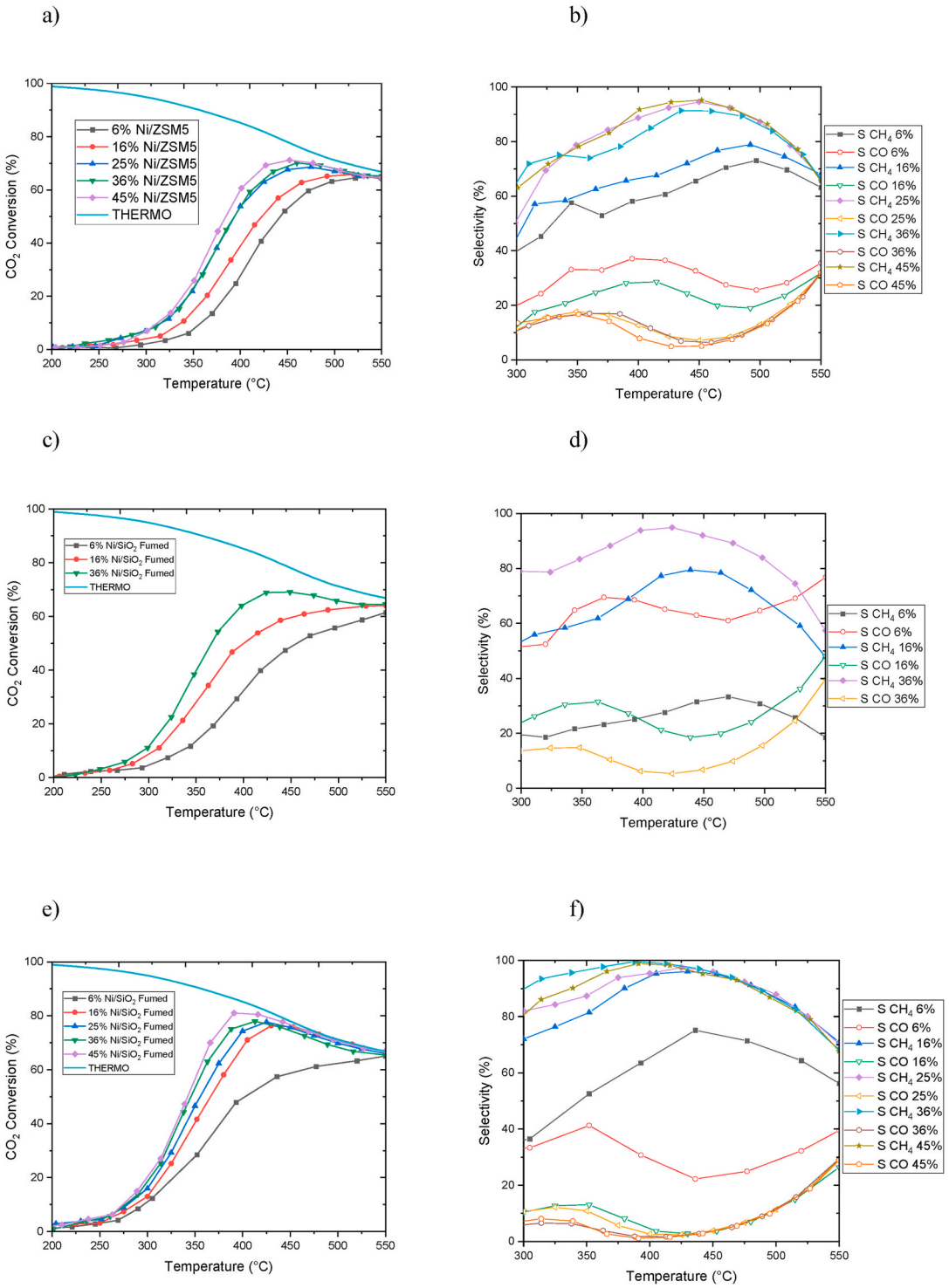

Fig. 19. Catalytic performance as a function of temperature: a) and b) ZSM-5, c) and d) SiO_2 Sigma, e) and f) SiO_2 Fumed as support.

with previous literature reports [92,93].

Detailed plots of conversion and selectivities of catalysts supported on SiO_2 Sigma are reported in Fig. 19c and d. Increasing the metal loading increased not only the performances of the catalysts, but selectivity towards CH_4 as well. It can be noted that the 6 % Ni/SiO_2 Sigma was very unselective, showing greater selectivity towards CO than towards CH_4, unlike for all other catalysts. 36 % Ni/SiO_2 (Sigma) showed the best performances of the series, reaching 69 % CO_2 conversion with 95 % CH_4 selectivity at 425 °C, insufficient for comparison with rival supports.

Conversion and selectivity for CH_4 and CO of all the catalysts supported on SiO_2 Fumed are reported in Fig. 19e and f. As in the previous case, increasing the metal loading improved both the conversion and the selectivity of the catalyst.

The difference in terms of catalytic activity between SiO_2 (Sigma) and SiO_2 (Fumed) is immediately noticeable. Fumed SiO_2 supported catalysts evidenced a greater surface area (approximately 200 $m^2\ g^{-1}$ vs. 4 $m^2\ g^{-1}$) and a total pore volume two orders of magnitude higher than those supported on SiO_2 Sigma.

However, when using a support with even higher surface area a corresponding further improvement of activity was not achieved. Indeed, a comparison of all the 36 % and 45 % Ni loaded catalysts is reported below (Fig. 20a and b). These were selected because they achieved the highest activity among this set of samples. 36 % Ni/SiO_2 Sigma and 45 % Ni/ZSM-5 showed very similar activities. Both series approach the thermodynamic equilibrium at 430/450 °C, compared to much lower temperature (390 °C, also characterized by higher conversion) achieved for the Fumed SiO_2 series. 36 % Ni/SiO_2 Fumed and 45 % Ni/SiO_2 Fumed displayed not only a greater activity, but a generally higher selectivity towards methane at every temperature, in particular in the 315–390 °C range compared to the 45 % Ni/SiO_2 Fumed catalyst.

Operating at low temperature favors the reaction from a thermodynamic point of view, allowing to minimize the RWGS reaction, but possibly favoring the production of coke through parasitic reactions, e.g. the Boudouard reaction. Higher Ni dispersion and reduced presence of large Ni crystals on the catalyst surface is usually beneficial to prevent coke accumulation in the form of nanotubes. The literature also confirms, for this and other reactions, that the presence of finely dispersed Ni particles, strongly interacting with the support, helps to reduce coke formation, increasing the selectivity towards methane. The carbon balances, especially for 36 % Ni/SiO_2 Fumed and 45 % Ni/SiO_2 Fumed, the two most active catalysts, showed values higher than 97 % at any temperature tested. Exceptions may arise at low conversion where the small amount of products and the small difference of CO_2 inlet and outlet flows leads to lower precision in the assessment of C balance.

A comparison with literature data is reported in Table 3 summarising Ni/SiO_2 catalysts used for CO_2 methanation mentioned in literature. Ye at [94]. synthesized a 40 % Ni/SiO_2 catalyst by impregnation. At a GHSW six times lower than the present case (i.e. much higher contact time) the catalyst showed conversion and selectivity of 70 and 90 % respectively at 450 °C. Catalysts prepared through ammonia evaporation method returned better performance with conversion and selectivity of 75 % and 90 % respectively.

Looking to characterization data it is evident that surface area and porosity alone are not determinant to achieve high activity. The role of the active phase is predominant, increasing both conversion and selectivity with increasing Ni loading. The support, not reactive for this set of formulations, exerts basically a structural role, but depending on its features it could determine different dispersion and interaction with the active phase. In the present case we have compared two pure silica supports, one amorphous with high surface area and mesoporosity, one with large particle size, highly crystalline structure and very low surface area and porosity and one silico-aluminate with well-developed regular crystallinity and uniform microporosity, together with the highest surface area. In this latter case a hetero-element was present, possibly imparting acidity to the prepared catalyst. Considering the EDS compositions reported in Table SI 2.2 (Supporting Information file) the ratio of Si/Al remained almost constant at variable Ni loading, indicating that surface deposition was not preferential on different sites of the zeolite.

Based on morphology and compositional data, Ni covered uniformly the surface available creating spherical nanoparticles or well developed bipyramid-shaped crystals over the support surface. In some cases 1D structures also formed, though their composition has not been fully elucidated. In the case of the zeolite support part of the Ni occluded the support pores, and its crystal sizes significantly increased with the loading. Also looking to the slightly lower reduction temperature of NiO when supported on ZSM-5, a lower interaction with the support may be inferred. By contrast, NiO particles with similar size supported over crystalline silica were much less reducible (and in turn demonstrated less active), due to a stronger metal-support interaction.

Therefore, in order to achieve satisfactory activity at low temperature, uniformly dispersed, well crystallised Ni particles are needed, acting as an independent phase with limited interaction with the support. The latter can help improving the dispersion to obtain a uniform array of nanoparticles, preventing also sintering, but it should not interact too strongly with the support inhibiting the redox cycles responsible of reactants activation. On the other hand, less interacting supports, even with much higher surface area are not satisfactory because they are not able to stabilize the formed Ni nanoparticles. Leading to their aggregation, as in the case of ZSM-5.

Based on the dependence on a critical Ni crystal size, it can be also supposed that structure sensitivity holds for this reaction.

Some analyses were also carried out on the spent catalysts, as allowed by the high dilution with SiC and the need for passivation of the downloaded exhaust material.

EDS analysis was performed on the spent catalysts loaded with 36 wt

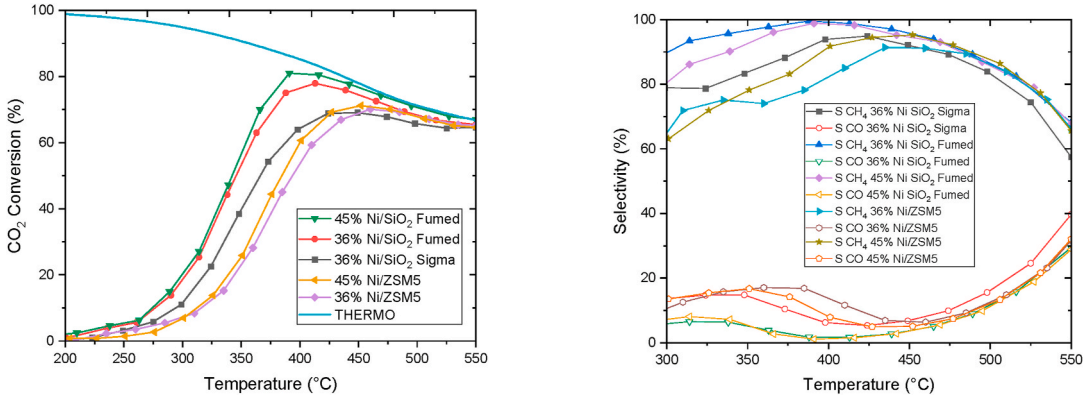

Fig. 20. (a) CO_2 conversion and (b) selectivity to CH_4 and CO of selected samples.

Table 3
Performance comparison of Ni-based catalyst for CO_2 methanation.

Catalyst	Synthesis	T_{red} (°C)	H_2/CO_2	Q_t/W (mL g^{-1} h^{-1})	T (°C)	Conv. CO_2 (%)	Sel. CH_4 (%)	Ref.
10 %Ni/SiO_2	Impregnation	500	4:1	120000	350	10	90	[95]
10 %Ni/SiO_2	Impregnation	400	4:1	3600	400	74	96	[96]
15 %Ni/SiO_2	Impregnation	400	4:1	60000	350	55	96	[97]
10 %Ni/SiO_2	Impregnation	500	4:1	2400 (h^{-1})	400	68	66	[98]
40 %Ni/SiO_2	Impregnation	500	4:1	10000	450	70	90	[94]
15 % Ni/ZSM-5	Impregnation	470	4:1	86200	450	68	94	[99]
10 % Ni/ZSM-5	Impregnation	500	4:1	2400	400	76	99	[98]
4.2 % Ni/ZSM-5	Vacuum-heating technique	500	4:1	30000	400	50	75	[100]
5 % Ni/ZSM-5	Impregnation	450	4:1	9000	450	75	90	[101]
15 % Ni/ZSM-5	Impregnation	570	4:1	12000	450	60	85	[97]
36 % Ni/ZSM-5	Impregnation	500	4:1	60000	460	70	91	[This work]
36 % Ni/SiO_2 (Sigma)	Impregnation	500	4:1	60000	424	69	95	[This work]
36 % Ni/SiO_2 (fumed)	Impregnation	500	4:1	60000	413	78	99	[This work]
45 % Ni/SiO_2 (fumed)	Impregnation	500	4:1	60000	390	81	99	[This work]

% Ni and for the SiO_2 Fumed with 45 wt% Ni content. The results are reported in Table SI 2.3. The Ni content remained approximately unchanged for the SiO_2 Fumed support (the apparent decrease is due to the local amount of C, not detected on the fresh catalyst and due in part to some CO_2 and CH_4 possibly adsorbed over the sample, but more likely due to the presence of SiC particles. The same samples also maintained the same morphology after use (Figures SI 5.1 and SI 5.2) and a uniform Ni distribution was evident in the EDS maps after use. The NiO whiskers disappeared after use, leaving a dispersed array of polyhedral particles.

The morphology and the Ni content were markedly different in the case of the SiO_2 Sigma and the ZSM-5 supports (Figures SI 5.3 and SI 5.4). A more significant decrease of the Ni amount was observed, likely due to surface reconstructuring after activation. Furthermore in the case of the ZSM-5 sample, SEM micrographs clearly evidenced the presence of irregularly sized Ni particles (20–150 nm) with a polyhedral shape.

4. Conclusions

Silica and ZSM-5 supported catalysts were prepared through wet impregnation of a Ni precursor. Different supports and metal loadings were used, yielding catalysts with different crystal phases, specific surface area, metal crystal size and metal-support interaction strength. All the as-prepared catalyst showed the presence of crystalline NiO, which reduced at variable temperature to Ni. Metal oxide reducibility was used as an index of metal dispersion (to be compared with morphology and crystal size) and of the interaction strength with the support. Characterisation of the spent catalysts revealed a morphological reconstruction of NiO, that in high loading samples was present in octahedral bipyramid shaped particles or even protruded as NiO whiskers. On the contrary, polyhedral particles were evident in the spent samples at high Ni content.

Activity tests have been conducted at atmospheric pressure. The bests results have been obtained at high Ni-loading with a pure Silica support. Significant differences between the use of SiO_2 Sigma and SiO_2 Fumed were found. The former, characterized mainly by a crystalline cristobalite phase showed a very low specific surface area, small pore volume and pore width, compared to the SiO_2 Fumed. Despite the extremely low pore volume of the SiO_2 Sigma, these catalysts behaved generally better than the ZSM-5 supported ones. A higher metal reducibility was correlated for all tests with a higher activity towards CO_2 methanation. The use of a support containing a small amount of aluminum, such as ZSM-5, did not improve the reactivity. Despite the extremely high SSA BET of the 36 % Ni/ZSM-5 sample, this catalyst was the one that performed worse than the pure silica supports at the same Ni loading. TPR analysis of low Ni loading catalysts supported on ZSM-5 showed a lower reduction temperature compared to the SiO_2 Fumed supported catalysts. For both series, increasing the loading led to the gradual increase in intensity of a peak at low reduction temperature, probably due to weakening of the interaction between the NiO and the support and to NiO particle size increase. At the highest metal concentration (45 wt% Ni) two separate reduction peaks were obtained.

The 36 % and 45 % Ni/SiO_2 Fumed showed the highest CO_2 conversion at 413 °C and 390 °C respectively with 99 % selectivity towards methane in both cases and of these, the 36 % Ni/SiO_2 Fumed allowed to achieve full selectivity toward methane at 390 °C. This promotes this material as extremely promising when compared with most catalysts reported in literature, combining the advantages associated with a simple synthesis methodology such as wet-impregnation of a commercial support with satisfactory performances obtained at high Qt/W, substantially reaching equilibrium conversion at low temperature. This demonstrates a methane productivity higher than most literature reports.

CRediT authorship contribution statement

Matteo Tommasi: Writing – original draft, Investigation, Data curation. **Alice Gramegna:** Software, Formal analysis. **Alessandro Di Michele:** Investigation. **Ermelinda Falletta:** Investigation, Data curation. **Federico Galli:** Supervision. **Laura Prati:** Writing – review & editing, Resources, Project administration, Funding acquisition. **Ceri Hammond:** Supervision, Resources, Project administration, Investigation, Funding acquisition, Conceptualization. **Ilenia Rossetti:** Writing – review & editing, Supervision, Resources, Project administration, Funding acquisition, Conceptualization.

Declaration of competing interest

The authors declare that they have no known competing financial interests or personal relationships that could have appeared to influence the work reported in this paper.

Acknowledgment

Special thanks are due to Lorenzo Rotasperti, Matteo Rotasperti and Elena Fiori for support in data collection and elaboration.

This study was carried out within the Agritech National Research Center and received funding from the European Union NextGenerationEU (PIANO NAZIONALE DI RIPRESA E RESILIENZA (PNRR) - MISSIONE 4 COMPONENTE 2, INVESTIMENTO 1.4 – D.D. 1032 17/06/2022, CN00000022). This manuscript reflects only the authors' views and opinions, neither the European Union nor the European Commission can be considered responsible for them. I. Rossetti and M. Tommasi acknowledge specifically the participation and funding of Tasks 8.2.3, 8.3.2 and 8.4.1.

This work has been also partially funded by the by the National Recovery and Resilience Plan (NRRP), Mission 4 Component 2

Investment 1.3—Call for tender No. 341 of 15.03.2022 of the Ministero dell'Università e della Ricerca (MUR); funded by the European Union NextGenerationEU, award number/project code PE0000021, Concession Decree No. 1561 of 11.10.2022 adopted by the Ministero dell'Università e della Ricerca (MUR), CUP D43C22003090001, project title "Network 4 Energy Sustainable Transition_NEST". In particular L. Prati gratefully acknowledges this funding.

A. Gramegna is grateful to Fondazione Cariplo for a research grant in the frame of the project "2021-0855 SCORE – Solar energy for circular CO_2 photoconversion and chemicals regeneration", in the frame of the 2021 call on circular economy.

L. Rotasperti, M. Rotasperti, I. Rossetti and C. Hammond gratefully acknowledge the Royal Society (UK) for funding a grant in the International Exchanges Scheme – Standard Programme 2019. This made possible the collection of DR-UV-Vis and Raman spectra.

Appendix A. Supplementary data

Supplementary data to this article can be found online at https://doi.org/10.1016/j.ijhydene.2025.04.217.

References

[1] Alfonso S, Gesto M, Sadoul B. Temperature increase and its effects on fish stress physiology in the context of global warming. J Fish Biol 2021;98:1496–508. https://doi.org/10.1111/jfb.14599.
[2] Ciscar J-CC. The impacts of climate change in Europe (the PESETA research project). Clim Change 2012;112:1–6. https://doi.org/10.1007/s10584-011-0336-x.
[3] Global Carbon Project. Global carbon budget | global carbon atlas. Glob Carbon Budg 2020;93. 2010-2019.
[4] International Energy Agency. CO 2 emissions in 2023. Int Energy Agency 2023;24:22.
[5] Hasan MMF, First EL, Boukouvala F, Floudas CA. A multi-scale framework for CO2 capture, utilization, and sequestration: CCUS and CCU. Comput Chem Eng 2015;81:2–21. https://doi.org/10.1016/j.compchemeng.2015.04.034.
[6] Theofanidis SA, Antzaras AN, Lemonidou AA. CO2 as a building block: from capture to utilization. Curr Opin Chem Eng 2023;39:100902. https://doi.org/10.1016/j.coche.2023.100902.
[7] Panzone C, Philippe R, Chappaz A, Fongarland P, Bengaouer A. Power-to-Liquid catalytic CO2 valorization into fuels and chemicals: focus on the Fischer-Tropsch route. J CO2 Util 2020;38:314–47. https://doi.org/10.1016/j.jcou.2020.02.009.
[8] Ren M, Zhang Y, Wang X, Qiu H. Catalytic hydrogenation of CO2 to methanol: a review. Catalysts 2022;12. https://doi.org/10.3390/catal12040403.
[9] Sholeha NA, Holilah H, Bahruji H, Ayub A, Widiastuti N, Ediati R, et al. Recent trend of metal promoter role for CO2 hydrogenation to C1 and C2+ products. South African J Chem Eng 2023;44:14–30. https://doi.org/10.1016/j.sajce.2023.01.002.
[10] Meiri N, Dinburg Y, Amoyal M, Koukouliev V, Nehemya RV, Landau MV, et al. Novel process and catalytic materials for converting CO2 and H2 containing mixtures to liquid fuels and chemicals. Faraday Discuss 2015;183:197–215. https://doi.org/10.1039/c5fd00039d.
[11] Shiva Kumar S, Lim H, Kumar SS, Lim H, Shiva Kumar S, Lim H. An overview of water electrolysis technologies for green hydrogen production. Energy Rep 2022;8:13793–813. https://doi.org/10.1016/j.egyr.2022.10.127.
[12] Zhou L. Progress and problems in hydrogen storage methods. Renew Sustain Energy Rev 2005;9:395–408. https://doi.org/10.1016/j.rser.2004.05.005.
[13] Wang H, Tong Z, Zhou G, Zhang C, Zhou H, Wang Y, et al. Research and demonstration on hydrogen compatibility of pipelines: a review of current status and challenges. Int J Hydrogen Energy 2022;47:28585–604. https://doi.org/10.1016/j.ijhydene.2022.06.158.
[14] Steinberger-Wilckens R, Sampson B. Market, commercialization, and deployment-toward appreciating total owner cost of hydrogen energy technologies. Elsevier Inc.; 2018. https://doi.org/10.1016/B978-0-12-814251-6.00008-3.
[15] El-Emam RS, Özcan H. Comprehensive review on the techno-economics of sustainable large-scale clean hydrogen production. J Clean Prod 2019;220:593–609. https://doi.org/10.1016/j.jclepro.2019.01.309.
[16] Yang H, Xu Z, Fan M, Gupta R, Slimane RB, Bland AE, et al. Progress in carbon dioxide separation and capture: a review. J Environ Sci 2008;20:14–27. https://doi.org/10.1016/S1001-0742(08)60002-9.
[17] Gkotsis P, Peleka E, Zouboulis A. Membrane-based technologies for post-combustion CO2 capture from flue gases: recent progress in commonly employed membrane materials. Membranes 2023;13:898. https://doi.org/10.3390/membranes13120898.
[18] Kintisch E. Can sucking CO2 out of the atmosphere really work? MIT Technol Rev; 2014. https://www.technologyreview.com/2014/10/07/171023/can-sucking-co2-out-of-the-atmosphere-really-work. [Accessed 30 September 2024].
[19] Flach C, Conti F, Bayraktar A, Goldbrunner M. Direct methanation and storage concepts for the flexibilization of biogas plants. Chem Eng Technol 2023;46:579–86. https://doi.org/10.1002/ceat.202200239.
[20] Awe OW, Zhao Y, Nzihou A, Minh DP, Lyczko N. A review of biogas utilisation, purification and upgrading technologies. Waste and Biomass Valorization 2017;8:267–83. https://doi.org/10.1007/s12649-016-9826-4.
[21] Tommasi M, Degerli SN, Ramis G, Rossetti I. Advancements in CO2 methanation: a comprehensive review of catalysis, reactor design and process optimization. Chem Eng Res Des 2024;201:457–82. https://doi.org/10.1016/j.cherd.2023.11.060.
[22] Calbry-Muzyka AS, Schildhauer TJ. Direct methanation of biogas—technical challenges and recent progress. Front Energy Res 2020;8. https://doi.org/10.3389/fenrg.2020.570887.
[23] Vogt C, Monai M, Kramer GJ, Weckhuysen BM. The renaissance of the Sabatier reaction and its applications on Earth and in space. Nat Catal 2019;2:188–97. https://doi.org/10.1038/s41929-019-0244-4.
[24] Alam MI, Cheula R, Moroni G, Nardi L, Maestri M. Mechanistic and multiscale aspects of thermo-catalytic CO2 conversion to C1 products. Catal Sci Technol 2021;11:6601–29. https://doi.org/10.1039/d1cy00922b.
[25] Zhang X, Zhang M, Zhang J, Zhang Q, Tsubaki N, Tan Y, et al. Methane decomposition and carbon deposition over Ni/ZrO2 catalysts: comparison of amorphous, tetragonal, and monoclinic zirconia phase. Int J Hydrogen Energy 2019;44:17887–99. https://doi.org/10.1016/j.ijhydene.2019.05.174.
[26] Compagnoni M, Tripodi A, Di Michele A, Sassi P, Signoretto M, Rossetti I. Low temperature ethanol steam reforming for process intensification: new Ni/MxO–ZrO2 active and stable catalysts prepared by flame spray pyrolysis. Int J Hydrogen Energy 2017;42:28193–213. https://doi.org/10.1016/j.ijhydene.2017.09.123.
[27] Gao J, Wang Y, Ping Y, Hu D, Xu G, Gu F, et al. A thermodynamic analysis of methanation reactions of carbon oxides for the production of synthetic natural gas. RSC Adv 2012;2:2358. https://doi.org/10.1039/c2ra00632d.
[28] Miguel CV, Soria MA, Mendes A, Madeira LM. Direct CO2 hydrogenation to methane or methanol from post-combustion exhaust streams - a thermodynamic study. J Nat Gas Sci Eng 2015;22:1–8. https://doi.org/10.1016/j.jngse.2014.11.010.
[29] Yarbaş T, Ayas N. A detailed thermodynamic analysis of CO2 hydrogenation to produce methane at low pressure. Int J Hydrogen Energy 2024;49:1134–44. https://doi.org/10.1016/j.ijhydene.2023.06.223.
[30] Ma V, Vannice MA. The catalytic synthesis of hydrocarbons from carbon monoxide and hydrogen. Catal Rev 1976;14:153–91. https://doi.org/10.1080/03602457608073410.
[31] Mills GA, Steffgen FW. Catalytic methanation. Catal Rev 1974;8:159–210. https://doi.org/10.1080/01614947408071860.
[32] Liu Q, Dong H. In situ immobilizing Ni nanoparticles to FDU-12 via trehalose with fine size and location control for CO2 methanation. ACS Sustainable Chem Eng 2020;8:2093–105. https://doi.org/10.1021/acssuschemeng.9b07004.
[33] Wu HC, Chang YC, Wu JH, Lin JH, Lin IK, Chen CS. Methanation of CO2 and reverse water gas shift reactions on Ni/SiO2 catalysts: the influence of particle size on selectivity and reaction pathway. Catal Sci Technol 2015;5:4154–63. https://doi.org/10.1039/c5cy00667h.
[34] Stangeland K, Kalai DY, Li H, Yu Z. Active and stable Ni based catalysts and processes for biogas upgrading: the effect of temperature and initial methane concentration on CO2 methanation. Appl Energy 2018;227:206–12. https://doi.org/10.1016/j.apenergy.2017.08.080.
[35] Fan WK, Tahir M. Recent trends in developments of active metals and heterogenous materials for catalytic CO2hydrogenation to renewable methane: a review. J Environ Chem Eng 2021;9:105460. https://doi.org/10.1016/j.jece.2021.105460.
[36] Rönsch S, Schneider J, Matthischke S, Schlüter M, Götz M, Lefebvre J, et al. Review on methanation - from fundamentals to current projects. Fuel 2016;166:276–96. https://doi.org/10.1016/j.fuel.2015.10.111.
[37] Calbry-Muzyka A, Madi H, Rüsch-Pfund F, Gandiglio M, Biollaz S. Biogas composition from agricultural sources and organic fraction of municipal solid waste. Renew Energy 2022;181:1000–7. https://doi.org/10.1016/j.renene.2021.09.100.
[38] Li L, Zeng W, Song M, Wu X, Li G, Hu C. Research progress and reaction mechanism of CO2 methanation over Ni-based catalysts at low temperature: a review. Catalysts 2022;12:244. https://doi.org/10.3390/catal12020244.
[39] Védrine JC. Importance, features and uses of metal oxide catalysts in heterogeneous catalysis. Chin J Catal 2019;40:1627–36. https://doi.org/10.1016/S1872-2067(18)63162-6.
[40] Shen L, Xu J, Zhu M, Han YF. Essential role of the support for nickel-based CO2 methanation catalysts. ACS Catal 2020;10:14581–91. https://doi.org/10.1021/acscatal.0c03471.
[41] Ashok J, Bian Z, Wang Z, Kawi S. Ni-phyllosilicate structure derived Ni-SiO2-MgO catalysts for bi-reforming applications: acidity, basicity and thermal stability. Catal Sci Technol 2018;8:1730–42. https://doi.org/10.1039/c7cy02475d.
[42] Choi DS, Kim NY, Yoo E, Kim J, Joo JB. Enhanced coke resistant Ni/SiO2@SiO2 core–shell nanostructured catalysts for dry reforming of methane: effect of metal-support interaction and SiO2 shell. Chem Eng Sci 2024;299:120480. https://doi.org/10.1016/j.ces.2024.120480.
[43] Albeladi N, Alsulami QA, Narasimharao K. Recent progress in nickel and silica containing catalysts for CO2 hydrogenation to CH4. Catalysts 2023;13. https://doi.org/10.3390/catal13071104.
[44] Weitkamp J. Catalytic hydrocracking—mechanisms and versatility of the process. ChemCatChem 2012;4:292–306. https://doi.org/10.1002/cctc.201100315.

[45] Olsbye U, Svelle S, Bjørgen M, Beato P, Janssens TVW, Joensen F, et al. Conversion of methanol to hydrocarbons: how zeolite cavity and pore size controls product selectivity. Angew Chemie Int Ed 2012;51:5810–31. https://doi.org/10.1002/anie.201103657.
[46] Deraz NM. The comparative jurisprudence of catalysts preparation methods: II. Deposition-precipitation and adsorption methods 2014;2.
[47] Lv C, Xu L, Chen M, Cui Y, Wen X, Li Y, et al. Recent progresses in constructing the highly efficient Ni based catalysts with advanced low-temperature activity toward CO2 methanation. Front Chem 2020;8:1–32. https://doi.org/10.3389/fchem.2020.00269.
[48] Le TA, Kang JK, Park ED. CO and CO2 methanation over Ni/SiC and Ni/SiO2 catalysts. Top Catal 2018;61:1537–44. https://doi.org/10.1007/s11244-018-0965-7.
[49] Cui Y, Chen B, Xu L, Chen M, Wu C, Qiu J, et al. CO2 methanation over the Ni-based catalysts supported on the hollow ZSM-5 zeolites: effects of the hollow structure and alkaline treatment. Fuel 2023;334:126783. https://doi.org/10.1016/j.fuel.2022.126783.
[50] Cychosz KA, Thommes M. Progress in the physisorption characterization of nanoporous gas storage materials. Engineering 2018;4:559–66. https://doi.org/10.1016/j.eng.2018.06.001.
[51] Al-Ghouti MA, Da'ana DA. Guidelines for the use and interpretation of adsorption isotherm models: a review. J Hazard Mater 2020;393:122383. https://doi.org/10.1016/j.jhazmat.2020.122383.
[52] Trepmann CA, Dellefant F, Kaliwoda M, Hess K, Schmahl WW, Hölzl S. Quartz and cristobalite ballen in impact melt rocks from the Ries impact structure, Germany, formed by dehydration of shock-generated amorphous phases. Meteorit Planet Sci 2020;55:2360–74. https://doi.org/10.1111/maps.13590.
[53] Maddalena R, Hall C, Hamilton A. Effect of silica particle size on the formation of calcium silicate hydrate [C-S-H] using thermal analysis. Thermochim Acta 2019;672:142–9. https://doi.org/10.1016/j.tca.2018.09.003.
[54] Shaaban ER, Kaid MA, Ali MGS. X-ray analysis and optical properties of nickel oxide thin films. J Alloys Compd 2014;613:324–9. https://doi.org/10.1016/j.jallcom.2014.06.057.
[55] Srivastava N, Srivastava PC. Realizing NiO nanocrystals from a simple chemical method. Bull Mater Sci 2010;33:653–6. https://doi.org/10.1007/s12034-011-0142-0.
[56] Liu C, Kang R, Bin F, Wei X, Hui KN, Kasipandi S, et al. Insights on copper, manganese, and Nickel/ZSM-5 catalytic mechanisms for nitric oxides selective reduction with ammonia. Carbon Resour Convers 2022;5:15–25. https://doi.org/10.1016/j.crcon.2021.11.002.
[57] Zhao Y, Qin X, Yao B, Gonzalez-Cortes S, Xiao T. Tailoring the crystallite size of Co3O4/SiO2 catalyst using organic-metal matrix method. Catal Today 2020;353:252–9. https://doi.org/10.1016/j.cattod.2018.06.050.
[58] Callister W. Microscope techniques. In: Materials science and engineering an introduction. seventh ed. John Wiley & Sons; 2006.
[59] Scimeca M, Bischetti S, Lamsira HK, Bonfiglio R, Bonanno E. Energy dispersive X-ray (EDX) microanalysis: a powerful tool in biomedical research and diagnosis. Eur J Histochem 2018;62:89–99. https://doi.org/10.4081/ejh.2018.2841.
[60] Tantawy MA, Shatat MR, El-Roudi AM, Taher MA, Abd-El-Hamed M. Low temperature synthesis of belite cement based on silica fume and lime. Int Sch Res Not 2014;2014:1–10. https://doi.org/10.1155/2014/873215.
[61] Saito S, Kurosawa K, Takemoto S. Growth of NiO whiskers by chemical transport. J Cryst Growth 1975;30:113–6. https://doi.org/10.1016/0022-0248(75)90209-2.
[62] Milewski JV, Whiskers. In: Concise encycl. Adv. Ceram. Mater. Elsevier; 1991. p. 516–9. https://doi.org/10.1016/B978-0-08-034720-2.50142-8.
[63] Jagtap P, Kumar P. Understanding whisker growth: effect of substrate and underlayer. In: Imaps 2016 - 49th int. Symp. Microelectron; 2016. Pasadena, CA USA.
[64] Wang Z, Wang S. Formation and evolution mechanism of metal whiskers in extreme aerospace environments: a review. Chin J Aeronaut 2023;36:1–13. https://doi.org/10.1016/j.cja.2023.07.007.
[65] Trisunaryanti W, Suarsih E, Triyono T, Falah II. Well-dispersed nickel nanoparticles on the external and internal surfaces of SBA-15 for hydrocracking of pyrolyzed α-cellulose. RSC Adv 2019;9:1230–7. https://doi.org/10.1039/C8RA09034C.
[66] Zhang X, Ding K, Gao X, Shi X, Han J, Pan J. Solid octahedral NiO micro-particles prepared by a calcination method in the presence of an ionic liquid and their application as anode for lithium ion batteries. Int J Electrochem Sci 2020;15:1498–508. https://doi.org/10.20964/2020.02.36.
[67] Kakherskyi S, Pshenychnyi R, Dobrozhan O, Vaziev JG, Bukivskii AP, Bukivskij PM, et al. Structural, microstructural, chemical, and optical properties of NiO nanocrystals and films obtained by 3D printing. Appl Phys A 2021;127:715. https://doi.org/10.1007/s00339-021-04847-5.
[68] Ascencio F, Bobadilla A, Escudero R. Study of NiO nanoparticles, structural and magnetic characteristics. Appl Phys A 2019;125:279. https://doi.org/10.1007/s00339-019-2579-8.
[69] Xing W, Zhang Y, Zhu J, Yu R. Structural and spin state transition in the polar NiO (1 1 1) surface. Appl Surf Sci 2020;532:147427. https://doi.org/10.1016/j.apsusc.2020.147427.
[70] Hermawan A, Hanindriyo AT, Ramadhan ER, Asakura Y, Hasegawa T, Hongo K, et al. Octahedral morphology of NiO with (111) facet synthesized from the transformation of NiOHCl for the NO x detection and degradation: experiment and DFT calculation. Inorg Chem Front 2020;7:3431–42. https://doi.org/10.1039/D0QI00682C.
[71] Kannan V, Inamdar AI, Pawar SM, Kim H-S, Park H-C, Kim H, et al. Facile route to NiO nanostructured electrode grown by oblique angle deposition technique for supercapacitors. ACS Appl Mater Interfaces 2016;8:17220–5. https://doi.org/10.1021/acsami.6b03714.
[72] Strohmeier B, White RG, Nunney TS, Mack P, Wright AE. Chemical characterization of material surfaces using X-ray photoelectron spectroscopy (XPS): the perfect complement to electron microscopy techniques. Microsc Microanal 2014;20:2062–3. https://doi.org/10.1017/S1431927614012045.
[73] Verma SK, Deb MK. Nondestructive and rapid determination of nitrate in soil, dry deposits and aerosol samples using KBr-matrix with diffuse reflectance Fourier transform infrared spectroscopy (DRIFTS). Anal Chim Acta 2007;582:382–9. https://doi.org/10.1016/j.aca.2006.09.020.
[74] Khairnar SD, Shrivastava VS. Facile synthesis of nickel oxide nanoparticles for the degradation of Methylene blue and Rhodamine B dye: a comparative study. J Taibah Univ Sci 2019;13:1108–18. https://doi.org/10.1080/16583655.2019.1686248.
[75] Hall DS, Lockwood DJ, Poirier S, Bock C, MacDougall BR. Raman and infrared spectroscopy of α and β phases of thin nickel hydroxide films electrochemically formed on nickel. J Phys Chem A 2012;116:6771–84. https://doi.org/10.1021/jp303546r.
[76] Saravanan S, Dubey RS. Synthesis of SiO2nanoparticles by sol-gel method and their optical and structural properties. Rom J Inf Sci Technol 2020;23:105–12.
[77] Udvardi B, Kovács IJ, Fancsik T, Kónya P, Bátori M, Stercel F, et al. Effects of particle size on the attenuated total reflection spectrum of minerals. Appl Spectrosc 2017;71:1157–68. https://doi.org/10.1177/0003702816670914.
[78] Narayanan S, Vijaya JJ, Sivasanker S, Ragupathi C, Sankaranarayanan TM, Kennedy LJ. Hierarchical ZSM-5 catalytic performance evaluated in the selective oxidation of styrene to benzaldehyde using TBHP. J Porous Mater 2016;23:741–52. https://doi.org/10.1007/s10934-016-0129-8.
[79] Biju V, Abdul Khadar M. Fourier transform infrared spectroscopy study of nanostructured nickel oxide. Spectrochim Acta Part A Mol Biomol Spectrosc 2003;59:121–34. https://doi.org/10.1016/S1386-1425(02)00120-8.
[80] Quindimil A, De-La-Torre U, Pereda-Ayo B, González-Marcos JA, González-Velasco JR. Ni catalysts with La as promoter supported over Y- and BETA- zeolites for CO2 methanation. Appl Catal B Environ 2018;238:393–403. https://doi.org/10.1016/j.apcatb.2018.07.034.
[81] Srinivas D, Satyanarayana CVV, Potdar HS, Ratnasamy P. Structural studies on NiO-CeO2-ZrO2 catalysts for steam reforming of ethanol. Appl Catal Gen 2003;246:323–34. https://doi.org/10.1016/S0926-860X(03)00085-1.
[82] Naresh G, Vijay Kumar V, Anjaneyulu C, Tardio J, Bhargava SK, Patel J, et al. Nano size Hβ zeolite as an effective support for Ni and Ni Cu for CO x free hydrogen production by catalytic decomposition of methane. Int J Hydrogen Energy 2016;41:19855–62. https://doi.org/10.1016/j.ijhydene.2016.09.131.
[83] Kim P, Kim Y, Kim H, Song IK, Yi J. Synthesis and characterization of mesoporous alumina with nickel incorporated for use in the partial oxidation of methane into synthesis gas. Appl Catal Gen 2004;272:157–66. https://doi.org/10.1016/j.apcata.2004.05.055.
[84] Abbas H, Nadeem K, Saeed N, Hassan A, Rahman S, Krenn H, et al. Photocatalytic activity and two-magnon behavior in nickel oxide nanoparticles with different silica concentration. J Appl Phys 2019;125. https://doi.org/10.1063/1.5083029.
[85] Mironova-Ulmane N, Kuzmin A, Steins I, Grabis J, Sildos I, Pärs M. Raman scattering in nanosized nickel oxide NiO. J Phys Conf Ser 2007;93. https://doi.org/10.1088/1742-6596/93/1/012039.
[86] Neuville DR, Charpentier T, Du JC, Yue YZ, Blanc W, Cicconi MR, et al. Structure characterizations and molecular dynamics simulations of melt, glass, and glass fibers. In: Fiberglass sci. Technol. Chem. Charact. Process. Model. Appl. Sustain. Cham: Springer International Publishing; 2021. p. 89–216. https://doi.org/10.1007/978-3-030-72200-5_2.
[87] Ghule AV, Ghule K, Punde T, Liu J-Y, Tzing S-H, Chang J-Y, et al. In situ monitoring of NiO–Al2O3 nanoparticles synthesis by thermo-Raman spectroscopy. Mater Chem Phys 2010;119:86–92. https://doi.org/10.1016/j.matchemphys.2009.07.050.
[88] Dietz RE, Parisot GI, Meixner AE. Infrared absorption and Raman scattering by two-magnon processes in NiO. J Appl Phys 1971;42:1484. https://doi.org/10.1063/1.1660309.
[89] George G, Anandhan S. Synthesis and characterisation of nickel oxide nanofibre webs with alcohol sensing characteristics. RSC Adv 2014;4:62009–20. https://doi.org/10.1039/C4RA11083H.
[90] Huang B, Li X, Ji S, Lang B, Habimana F, Li C. Effect of MgO promoter on Ni-based SBA-15 catalysts for combined steam and carbon dioxide reforming of methane. J Nat Gas Chem 2008;17:225–31. https://doi.org/10.1016/S1003-9953(08)60055-9.
[91] Rossetti I, Biffi C, Bianchi CL, Nichele V, Signoretto M, Menegazzo F, et al. Ni/SiO 2 and Ni/ZrO 2 catalysts for the steam reforming of ethanol. Appl Catal B Environ 2012;117–118:384–96. https://doi.org/10.1016/j.apcatb.2012.02.006.
[92] Myronyuk IF, Mandzyuk VI, Sachko VM, Gun'ko VM. Structural and morphological features of disperse alumina synthesized using aluminum nitrate nonahydrate. Nanoscale Res Lett 2016;11:153. https://doi.org/10.1186/s11671-016-1366-0.
[93] Martínez J, Hernández E, Alfaro S, López Medina R, Valverde Aguilar G, Albiter E, et al. High selectivity and stability of nickel catalysts for CO2 methanation: support effects. Catalysts 2018;9:24. https://doi.org/10.3390/catal9010024.
[94] Ye RP, Gong W, Sun Z, Sheng Q, Shi X, Wang T, et al. Enhanced stability of Ni/SiO2 catalyst for CO2 methanation: derived from nickel phyllosilicate with strong metal-support interactions. Energy 2019;188:116059. https://doi.org/10.1016/j.energy.2019.116059.

[95] Wu HC, Chang YC, Wu JH, Lin JH, Lin IK, Chen CS. Methanation of CO 2 and reverse water gas shift reactions on Ni/SiO 2 catalysts: the influence of particle size on selectivity and reaction pathway. Catal Sci Technol 2015;5:4154–63. https://doi.org/10.1039/C5CY00667H.
[96] Chen Y, Qiu B, Liu Y, Zhang Y. An active and stable nickel-based catalyst with embedment structure for CO2 methanation. Appl Catal B Environ 2020;269: 118801. https://doi.org/10.1016/j.apcatb.2020.118801.
[97] Cui Y, Qiu J, Chen B, Xu L, Chen M, Wu C, et al. CO2 methanation over Ni/ZSM-5 catalysts: the effects of support morphology and La2O3 modification. Fuel 2022; 324:124679. https://doi.org/10.1016/j.fuel.2022.124679.
[98] Guo X, Traitangwong A, Hu M, Zuo C, Meeyoo V, Peng Z, et al. Carbon dioxide methanation over nickel-based catalysts supported on various mesoporous material. Energy & Fuels 2018;32:3681–9. https://doi.org/10.1021/acs.energyfuels.7b03826.
[99] Bacariza MC, Maleval M, Graça I, Lopes JM, Henriques C. Power-to-methane over Ni/zeolites: influence of the framework type. Microporous Mesoporous Mater 2019;274:102–12. https://doi.org/10.1016/j.micromeso.2018.07.037.
[100] Yan P, Peng H, Wu X, Rabiee H, Weng Y, Konarova M, et al. Impact of varied zeolite materials on nickel catalysts in CO2 methanation. J Catal 2024;432: 115439. https://doi.org/10.1016/j.jcat.2024.115439.
[101] da Costa-Serra JF, Cerdá-Moreno C, Chica A. Zeolite-supported Ni catalysts for CO2 methanation: effect of zeolite structure and Si/Al ratio. Appl Sci 2020;10: 5131. https://doi.org/10.3390/app10155131.